# Molecular basis for plasma membrane recruitment of PI4KA by EFR3

Sushant Suresh[1]*, Alexandria L Shaw[1,2]*, Joshua G Pemberton[3,4], Mackenzie K Scott[1], Noah J Harris[1], Matthew AH Parson[1], Meredith L Jenkins[1], Poojah Rohilla[3], Alejandro-Alvarez-Prats[3], Tamas Balla[3], Calvin K Yip[2#], John E Burke[1,2#]

[1] Department of Biochemistry and Microbiology, University of Victoria, Victoria, BC, V8W 2Y2, Canada

[2] Department of Biochemistry and Molecular Biology, The University of British Columbia, Vancouver, BC, V6T 1Z3, Canada

[3] Section on Molecular Signal Transduction, Eunice Kennedy Shriver National Institute of Child Health and Human Development, National Institutes of Health, Bethesda, MD, United States.

[4] Current address: Department of Biology, Western University, London, ON, N6A 3K7 Canada

* These authors contributed equally

[#]Corresponding authors: Calvin K Yip calvin.yip@ubc.ca, John E Burke jeburke@uvic.ca: Lead contact: John E Burke jeburke@uvic.ca

**Abstract**

The lipid kinase phosphatidylinositol 4 kinase III alpha (PI4KIIIα/PI4KA) is a master regulator of the lipid composition and asymmetry of the plasma membrane. PI4KA exists primarily in a heterotrimeric complex with its regulatory proteins TTC7 and FAM126. Fundamental to PI4KA activity is its targeted recruitment to the plasma membrane by the lipidated proteins EFR3A and EFR3B. Here, we report a cryo-EM structure of the C-terminus of EFR3A bound to the PI4KA-TTC7B-FAM126A complex, with extensive validation using both hydrogen deuterium exchange mass spectrometry (HDX-MS), and mutational analysis. The EFR3A C-terminus undergoes a disorder-order transition upon binding to the PI4KA complex, with an unexpected direct interaction with both TTC7B and FAM126A. Complex disrupting mutations in TTC7B, FAM126A, and EFR3 decrease

PI4KA recruitment to the plasma membrane. Multiple post-translational modifications and disease linked mutations map to this site, providing insight into how PI4KA membrane recruitment can be regulated and disrupted in human disease.

**One sentence summary**

The cryo-EM structure of the C-terminus of EFR3A bound to the PI4KA complex reveals the molecular mechanism underlying PI4KA membrane localisation, and provides novel insight into PI4KA regulation and its involvement in human disease.

## Introduction

Phosphoinositide lipids play numerous roles in myriad cellular functions (*1–3*). One of the most abundant phosphoinositide lipids is the molecule phosphatidylinositol 4-phosphate (PI4P) (*4*), which can be generated by four different lipid kinases in humans (encoded by the genes *PI4KA, PI4KB, PI4K2A,* and *PI4K2B*), with PI4KA generating the primary pool of PI4P at the plasma membrane (PM) (*5*). PI4P is essential for defining the identity of the PM, as it is the precursor for the signaling lipids phosphatidylinositol (4,5)-bisphosphate (PI(4,5)$P_2$) and phosphatidylinositol (3,4,5)-trisphosphate ($PIP_3$), regulates the non-vesicular transport of phosphatidylserine (*6*), and is also a substrate of the phospholipase C (PLC) pathway (*7*). Dysregulation of PI4KA is involved in multiple human diseases (*8*), with loss of function mutations in PI4KA or its regulatory proteins being causative of neurological (*9*, *10*), immunological (*11*), and gastrointestinal disorders (*12*). PI4KA and its regulatory proteins have also been shown to be critical for cancer growth (*13*, *14*) and viral infection (*15*).

PI4KA shares an evolutionary history with the class I-III PI 3-kinases (PI3Ks) and PI4KB, with a central feature of regulation for all of these enzymes being that they are recruited to membrane surfaces by specific lipid or protein binding partners (*16*). PI4KA primarily exists in cells as a complex with the regulatory proteins TTC7 (two isoforms TTC7A and TTC7B) and FAM126 (two isoforms FAM126A and FAM126B) (*17*, *18*). PI4KA and TTC7 are conserved throughout all eukaryotes, while FAM126 is found in most metazoans, but is lost in simpler basal eukaryotes (*19*). Analysis of the PI4KA-TTC7-

60 FAM126 complex using cryogenic electron microscopy (cryo-EM) and hydrogen
61 deuterium exchange mass spectrometry (HDX-MS) showed that it assembles into a large
62 ~750 kDa complex (*17*, *20*). PI4KA self-assembles through its dimerization domain
63 leading to a dimer of heterotrimers, which we will refer to as the PI4KA complex. FAM126
64 does not bind to PI4KA directly but instead acts as a stabilizer of TTC7, which binds to
65 PI4KA (*18*). The most well-established mechanism of membrane recruitment is through
66 the binding of the palmitoylated protein EFR3 to TTC7 (*5*). However, the exact molecular
67 mechanism underlying EFR3-mediated PM recruitment of the PI4KA complex has
68 remained elusive (*5*, *21*, *22*).

69 The interaction between EFR3 and TTC7 has been extensively studied in yeast,
70 where the protein Ypp1 (yeast ortholog of TTC7) binds to the disordered C-terminus of
71 Efr3 (yeast homolog of EFR3) (*23*, *24*). In yeast, this interaction is regulated by
72 phosphorylation of the Efr3 C-terminus, with phosphorylation disrupting Ypp1-mediated
73 PM recruitment of Stt4 (yeast homolog of PI4KA) (*24*). It has been challenging to
74 extrapolate these results to derived eukaryotic lineages, including humans, as the C-
75 terminus of EFR3 is only partially evolutionarily conserved. As PI4KA activity needs to be
76 upregulated upon PLC signaling to maintain the PM pool of PI4P (*25*), there likely are
77 unknown regulatory mechanisms controlling EFR3-mediated recruitment in more
78 complex vertebrate cell models. Defining the molecular mechanism of EFR3-mediated
79 PM recruitment of PI4KA is essential to understanding possible regulatory mechanisms
80 controlling the activity of the PI4KA complex through association with the PM.

81 To fully explore the molecular mechanisms of how EFR3 can bind to and regulate
82 the PI4KA complex we have utilized a synergistic application of cryo-EM and HDX-MS.
83 Our structural analyses reveal that EFR3A interacts with the PI4KA complex through an
84 evolutionarily conserved region within the C-terminus of EFR3A. Unexpectedly, the C-
85 terminus of EFR3A forms an extended helical interface toward both TTC7B and
86 FAM126A. This interface was validated by both HDX-MS and mutational analysis. The
87 development of a live-cell bioluminescence resonance-energy transfer (BRET)-based
88 assay of PI4KA recruitment to the PM as well as confocal imaging show the key functional
89 role of the EFR3 C-terminus in membrane recruitment of the PI4KA complex. Overall, our

90 findings provide useful insight into the molecular and structural basis of PI4KA regulation
91 at the PM.
92
93 **Results**
94 *Cryo-EM analysis of the EFR3A-PI4KA complex*
95 Investigation into the molecular basis of how EFR3A regulates PI4KA required the
96 production of a stable PI4KA-TTC7B-FAM126A complex. This was achieved by co-
97 expression of full-length PI4KA and TTC7B, together with a truncated FAM126A lacking
98 the disordered C-terminus (1-308, FAM126A ΔC) (**Fig. 1A**). This complex has been
99 structurally characterized (*17*), is homogenous, and elutes off gel filtration consistent with
100 the formation of a dimer of heterotrimers. For simplicity, this complex will be referred to
101 as the PI4KA complex throughout the manuscript. It has previously been established that
102 in yeast the disordered C-terminus of EFR3 mediates recruitment of the TTC7 ortholog
103 Ypp1 (*24*). To identify the related site in human EFR3A we carried out a bioinformatic
104 analysis of sequence conservation. While there were no regions that were strictly
105 conserved between yeast and humans (**Supplemental Fig 1)**, there was a region that
106 was highly conserved between chordates in the C-terminus. We generated multiple
107 constructs spanning this region for expression in *E. coli*, with the most stable and
108 homogenous being a construct spanning residues 721-791 of EFR3A (**Fig. 1A**).
109 To validate that this EFR3A fragment could interact with the PI4KA complex, size
110 exclusion chromatography was used to determine whether complex formation would
111 occur. When co-incubated together, the PI4KA complex co-eluted with the EFR3A C-
112 terminal fragment, with elution volume and SDS-PAGE analysis consistent with a dimer
113 of hetero-tetramers (**Fig. 1B**). We then carried out cryo-EM analysis of this reconstituted
114 complex. While the protein specimen appeared homogeneous on negative stain EM
115 grids, vitrification of this protein product yielded aggregated particles at the air-water
116 interface. To address this problem, we subjected the complex to limited $BS^3$ chemical
117 crosslinking followed by size exclusion chromatography.
118 Using this sample, we were able to generate a cryo-EM reconstruction of the
119 PI4KA complex bound to the C-terminus of EFR3A at a nominal resolution of 3.63Å from

120 67,563 particles (**Fig. 1C, Supplemental Fig 2**). Refinement yielded large differences in
121 local resolution between the two hetero-tetramers. We will therefore focus our
122 descriptions on the better-resolved hetero-tetramer within the assembly. (**Supplemental**
123 **Fig 2C**). Unexpectedly, our structure showed that the EFR3A C-terminus binds to both
124 TTC7B and FAM126A, forming a V-shape composed of three alpha helices. The local
125 resolution of the first interface $\alpha$-helix in EFR3A spanning residues 728-735 was sufficient
126 for unambiguous manual model building into density (**Supplemental Fig 3**), with
127 AlphaFold Multimer (*26*, *27*) and manual model building allowing for building the 2$^{nd}$ and
128 3$^{rd}$ $\alpha$-helices (**Supplemental Fig 3**). Overall, we were able to build a molecular model of
129 residues 724-787 of EFR3A bound to TTC7B-FAM126A (**Fig. 1D**). No direct interactions
130 were seen between the EFR3A C-terminus and PI4KA, with no major conformational
131 changes in the PI4KA subunit. The interface between EFR3A and FAM126A was
132 unexpected, as both EFR3 and TTC7 are conserved from yeast to humans, while
133 FAM126 is only conserved in metazoans (*19*).

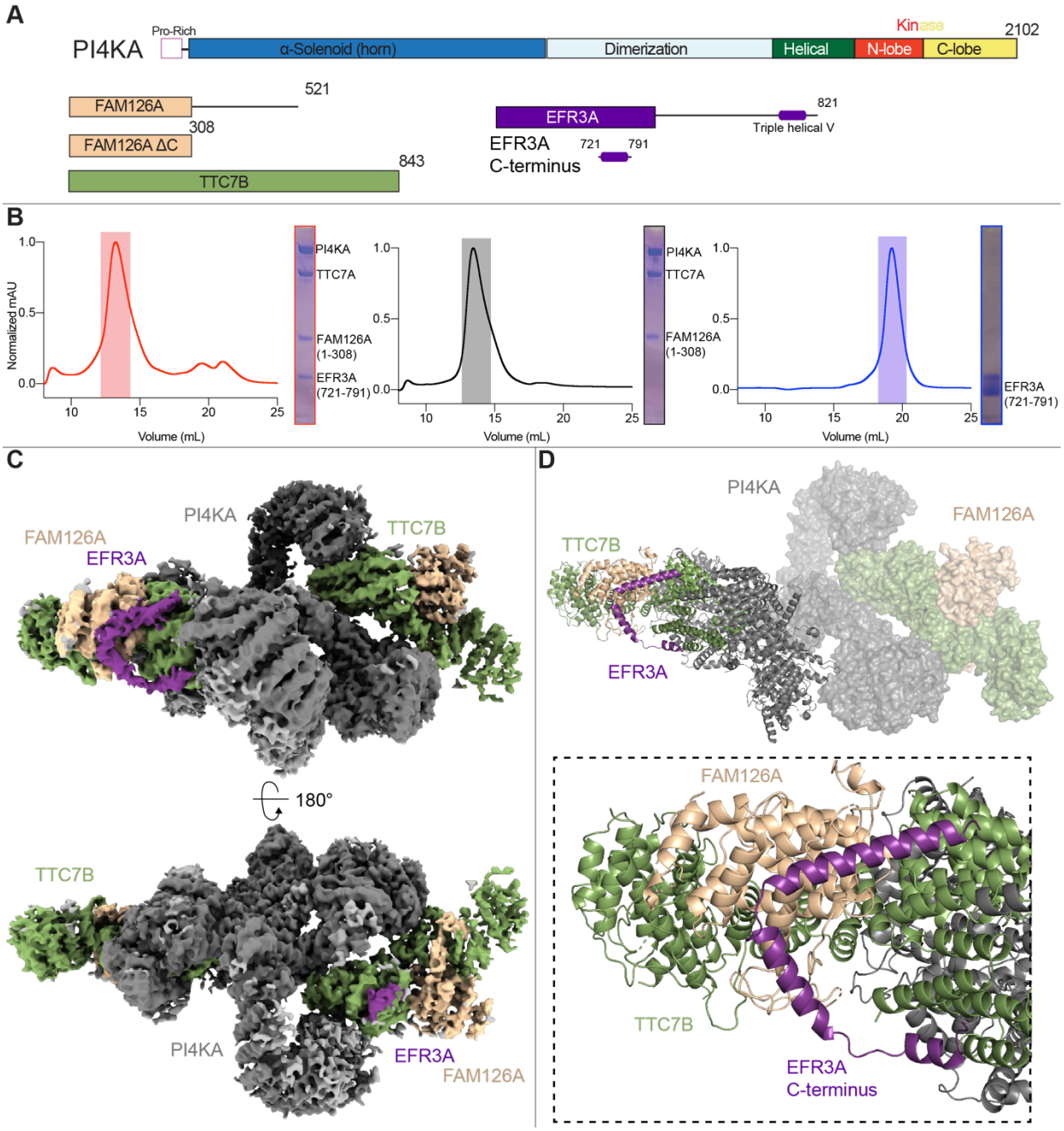


**Figure 1. Cryo-EM analysis of EFR3 binding to the PI4KA complex**

**A.** Domain schematics of the full-length PI4KA complex and EFR3A constructs used in this paper. Constructs used in this paper are PI4KA/TTC7B/FAM126A ΔC (referred to as PI4KA complex) and EFR3A (721-791) referred to as EFR3A.

**B.** Size exclusion chromatography traces of (L) PI4KA complex/EFR3A, (M) PI4KA complex, and (R) EFR3A, with corresponding SDS-PAGE gels to show protein present in the highlighted size exclusion chromatography (SEC) peaks.

142 **C.** Cryo-EM density map of the PI4KA complex bound to EFR3A. EFR3A was bound to both sides of the
143 hetero-trimer, however, the full triple helical V was only visible in one of the two dimers of hetero-
144 tetramers (see left side of the molecule in the top panel).
145 **D.** Molecular model of the triple helical V in the C-terminus of EFR3A (724-787) bound to the PI4KA
146 complex, with a zoom-in highlighting EFR3A contacts with both TTC7B and FAM126A.
147

148 *HDX-MS analysis of the EFR3A-PI4KA complex*

149 To further understand the dynamics of the interaction between the PI4KA complex
150 and EFR3A, we employed HDX-MS, a powerful technique to investigate protein
151 conformational dynamics (*28–30*). HDX-MS experiments were performed on the PI4KA
152 complex with and without EFR3A. Deuterium incorporation was measured over a range
153 of time points (30s, 300s, 3000s, 10000s) and the mass shift upon deuterium
154 incorporation were analyzed via mass spectrometry, with significant differences in
155 exchange being defined as changes greater than >0.45 Da and >5% at any time point
156 with unpaired t-test values of $p<0.01$.

157 Multiple regions in both TTC7B and FAM126A showed significant decreases in
158 exchange upon binding to EFR3A. These regions included residues 89-102 in FAM126A
159 and residues 539-544 in TTC7B (**Fig. 2A+B, Supplemental Fig 4**), which were all
160 localized at the interface observed by cryo-EM. No significant changes in exchange were
161 observed in PI4KA, consistent with the lack of direct contacts observed in the cryo-EM
162 structure.
163

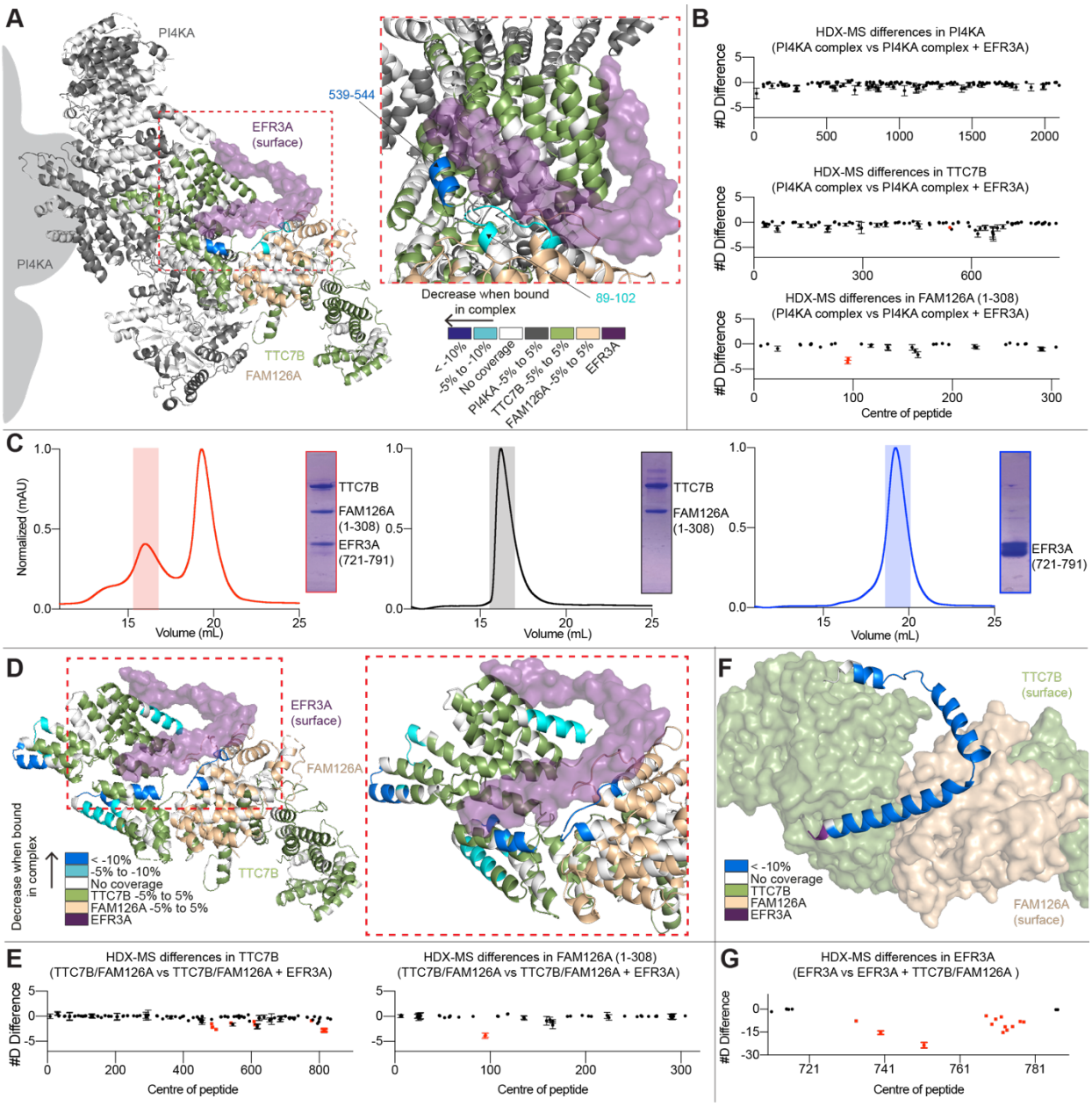


**Figure 2: HDX-MS analysis of the interaction of EFR3A with TTC7B and FAM126A**

**A.** Residues showing significant differences in deuterium exchange (defined as >5% 0.45 Da, and p>0.01 in an unpaired two-tailed t-test at any time point) upon PI4KA complex binding to EFR3A. Differences are mapped on a structural model of the high local resolution half, with a zoom-in on the interface. Differences are indicated by the legend.

**B.** Sum of the number of deuteron differences of PI4KA complex upon formation with EFR3A analysed over the entire deuterium exchange time course for the PI4KA complex. Each point is representative of the centre residue of an individual peptide. Peptides that met the significance criteria described in A are

173 coloured red. Error is shown as the sum of standard deviations across all 4 time points (SD) (n=3 for each
174 condition in each timepoint).
175 **C.** Size exclusion chromatography traces of (L) TTC7B-FAM126A ΔC -EFR3A, (M) TTC7B-FAM126A
176 ΔC, and (R) EFR3A, with corresponding SDS-PAGE gels to show protein present in the highlighted SEC
177 peaks.
178 **D.** TTC7B-FAM126A residues showing significant differences in deuterium exchange (defined as >5%
179 0.45 Da, and p>0.01 in an unpaired two-tailed t-test at any time point) upon formation of the TTC7B-
180 FAM126A-EFR3A complex. Differences are mapped on a structural model of the high local resolution half
181 removing PI4KA, with a zoom in on the interface. Differences are indicated by the legend.
182 **E.** Sum of the number of deuteron difference of TTC7B and FAM126A upon complex formation with
183 EFR3A analysed over the entire deuterium exchange time course for the dimer. Each point is
184 representative of the centre residue of an individual peptide. Peptides that met the significance criteria
185 described in A are coloured red. Error is shown as the sum of standard deviations across all 5 time points
186 (SD) (n=3 for each condition in each timepoint).
187 **F.** EFR3A residues showing significant differences in deuterium exchange (defined as >5% 0.45 Da, and
188 p>0.01 in an unpaired two-tailed t-test at any time point) upon formation of the TTC7B-FAM126A-EFR3A
189 complex. Differences are mapped on a structural model of the high local resolution half removing PI4KA
190 zooming in on the interface. Differences are indicated by the legend. The construct used has overlapping
191 MBP peptides that do not contain EFR3A residues, therefore peptides that start before 721 are not
192 EFR3A sequence.
193 **G.** Sum of the number of deuteron difference of EFR3A upon complex formation with TTC7B-FAM126A
194 analysed over the entire deuterium exchange time course for the EFR3A. Each point is representative of
195 the centre residue of an individual peptide. Peptides that met the significance criteria described in A are
196 coloured red. Error is shown as the sum of standard deviations across all 4 time points (SD) (n=3 for each
197 condition in each timepoint). Individual deuterium exchange curves for significant differences for all
198 conditions are shown in Supplemental Fig 4.
199

200 Together, the cryo-EM and HDX-MS data suggested that EFR3A would bind
201 similarly to an isolated dimer of TTC7B-FAM126A ΔC. We purified TTC7B-FAM126A ΔC,
202 which will be referred to as TTC7B-FAM126A, from *E. coli*, with gel filtration profiles in the
203 presence of the C-terminus of EFR3A consistent with the formation of a stable trimer (**Fig.
204 2C**). To investigate the implications of the lack of PI4KA on conformational dynamics, we
205 utilized HDX-MS to compare TTC7B-FAM126A in the presence and absence of the C-
206 terminus of EFR3A. HDX-MS experiments were measured over 5 time points (3s, 30s,

207 300s, 3000s and 10,000s at 18°C). We observed significant decreases in HDX in the
208 same sites on TTC7B and FAM126A as observed in the PI4KA complex, with additional
209 regions spanning the entire EFR3A interface, as well as some allosteric differences
210 distant from the EFR3A binding site (**Fig. 2D-E, Supplemental Fig 4**). To map changes
211 in deuterium incorporation in EFR3A, we utilized a different EFR3A C-terminus construct
212 containing residues 721-791 of EFR3A with an N-terminal maltose binding protein (MBP)
213 tag, with HDX-MS experiments performed on MBP-EFR3A apo and in complex with
214 TTC7B-FAM126A. Deuterium incorporation was measured over 4 time points (3s, 30s,
215 300s at 18°C and 3s at 0°C). Peptides spanning all three helices in EFR3A showed a
216 significant decrease in HDX, further validating the interface observed in the cryo-EM
217 structure (**Fig. 2F-G, Supplemental Fig 4**). We carried out biolayer interferometry (BLI)
218 measurements of TTC7B-FAM126A binding to the C-terminus of EFR3A, with this
219 interface having a $K_D$ of ~250 nM (**Fig. 3A**).
220
221 *Molecular details of the EFR3A interface with TTC7B*
222 Our cryo-EM structure revealed that EFR3A engages TTC7B and FAM126A in an
223 extended interface composed of three α-helices from EFR3A oriented in a V, resulting in
224 a buried surface area of ~1500 Å$^2$. This interface is primarily hydrophobic, with the
225 interface between EFR3A and TTC7B being ~800 Å$^2$ and is composed of the first EFR3A
226 α-helix (residues 728-735), and the latter half of the 3$^{rd}$ EFR3A α-helix (761-785) (**Fig.
227 3B-C**). The first α-helix is likely the most stable as this is the only region of EFR3A visible
228 in both halves of the cryo-EM map and is also the region with the highest local resolution
229 in the electron density (**Fig 2C**). The α1-helix in EFR3A is amphipathic, with the
230 hydrophobic face interacting with primarily hydrophobic residues in three helices in
231 TTC7B (residues 599-616, 690-707, and 712-723). The interacting residues in the α1 and
232 α3 helices of EFR3A are strongly conserved throughout evolution in vertebrates, with
233 partial conservation in metazoans, and very limited conservation in yeast (**Fig 3B and
234 Supplemental Fig 1**). There are some notable differences in interfacial residues between
235 EFR3A and EFR3B that may alter binding affinity, potentially highlighting isoform-specific
236 regulatory differences.

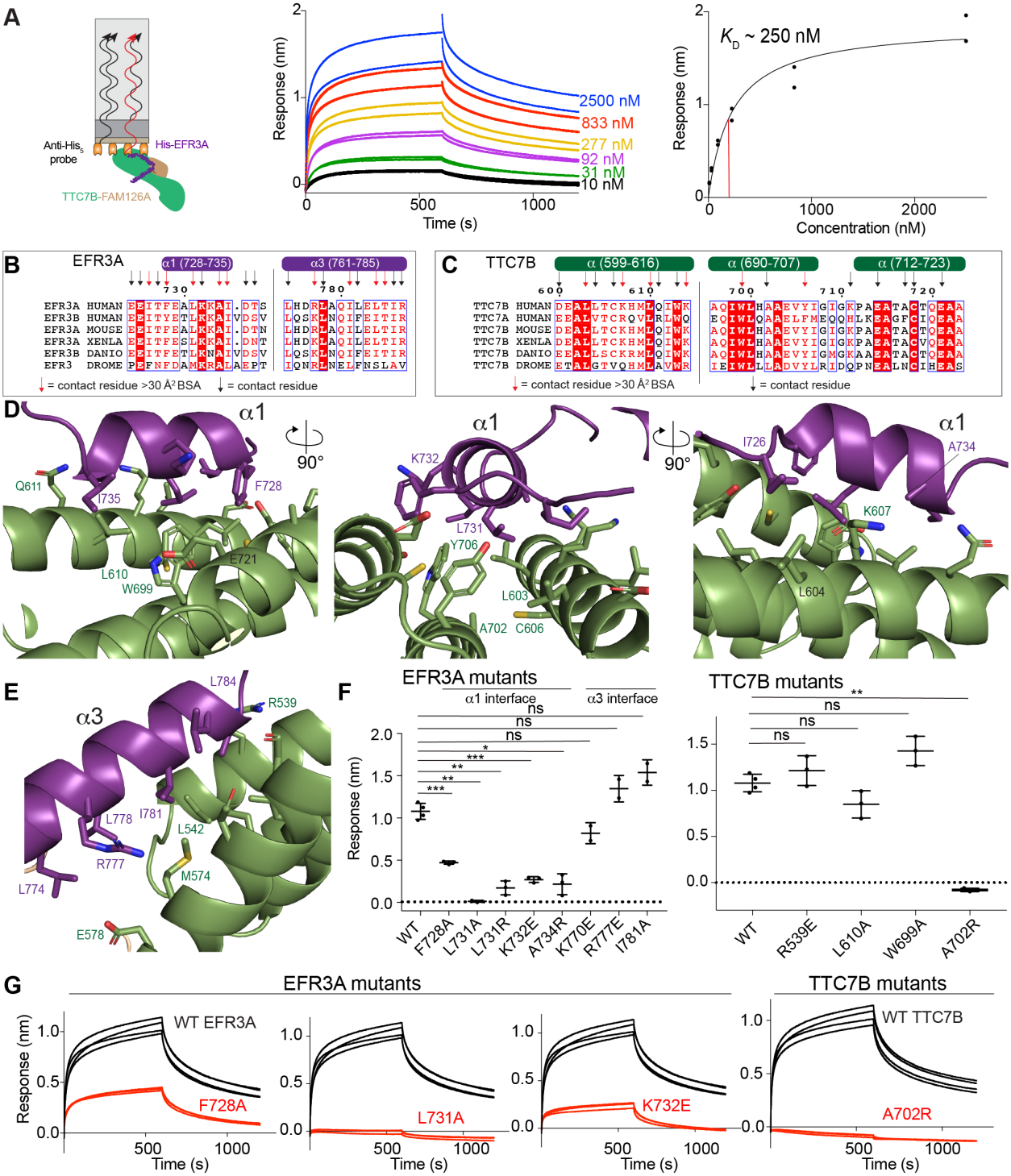


**Figure 3: Molecular basis of EFR3A binding to TTC7B**

**A.** Cartoon schematic (L) of a bio-layer interferometry (BLI) experiment showing binding of immobilized His-EFR3A (721-791) to TTC7B-FAM126A. Association and dissociation curves (M) for the binding of His-EFR3A (721-791) to different concentrations of TTC7B-FAM126A (10-2500 nM). The experiment was carried out in duplicate, with all data shown. Normalized BLI response versus concentration of TTC7B-

243 FAM126A (R), with $K_D$ estimated by one site specific non-linear regression. Each data point is shown
244 (n=2).
245 **B.** Multiple sequence alignment of EFR3A from *Homo sapiens, Mus musculus, Xenopus laevis, Danio*
246 *rerio, Drosophila melanogaster*. EFR3A secondary structure of α1 and α3 helices are annotated above
247 the alignment. Contact residues within 6 Å of TTC7B are annotated using arrows. Contact residues with
248 BSA > 30 $Å^2$ are annotated using red arrows.
249 **C.** Multiple sequence alignment of TTC7B from *Homo sapiens, Mus musculus, Xenopus laevis, Danio*
250 *rerio, Drosophila melanogaster*. TTC7B secondary structure is annotated above the alignment. Contact
251 residues within 6 Å of EFR3A are annotated using arrows. Contact residues with BSA > 30 $Å^2$ are
252 annotated using red arrows.
253 **D.** Zoomed in cartoon view of the EFR3A α1-TTC7B interface with putative interfacial residues labelled.
254 EFR3A and TTC7B are coloured according to in-figure text.
255 **E.** Zoomed in cartoon view of the EFR3A α3-TTC7B interface with putative interfacial residues labelled.
256 EFR3A and TTC7B are coloured according to in-figure text.
257 **F.** Maximum BLI response of various EFR3A and TTC7B mutants compared to WT. Error is shown as
258 standard deviation (n=3) with two-tailed p values indicated as follows: **p<0.001; ***p<0.0001; not
259 significant (ns) > 0.01.
260 **G.** Raw BLI association and dissociation curves of EFR3A and TTC7B mutants compared to WT. His-
261 EFR3A was loaded on the anti-penta-His tip at 200 nM and dipped in TTC7B-FAM126A at 500 nM. Raw
262 BLI curves of all mutants in Supplemental Fig 5.
263
264 We generated several point mutations on both EFR3A and TTC7B and used Bio-
265 Layer Interferometry (BLI) to determine their effect on complex formation (**Fig 3F-G and**
266 **Supplemental Fig 5**). Mutation of residues in the α1 helix in EFR3A, including F728A,
267 L731A, K732E, and A734R led to decreased binding, with the L731A mutation causing
268 the largest disruption. Mutation of a corresponding residue in TTC7B (A702R) also led to
269 an almost complete disruption of EFR3A binding, with removal of hydrophobic residues
270 showing a minimal effect on binding affinity. Mutations of residues in the α3 helix of
271 EFR3A, or corresponding residues in TTC7B showed no significant effect on binding,
272 highlighting that the α1 helix of EFR3A is indispensable for binding, with a limited role of
273 the C-terminal half of the α3 helix in EFR3A.
274
275 *Molecular details of the EFR3A interface with FAM126A*

It was unexpected that there would be an extensive interface between EFR3A and FAM126A, as FAM126A has not been previously annotated as a critical partner in EFR3-mediated PM recruitment of PI4KA. There is an extended evolutionarily conserved interface between EFR3A and FAM126A (**Fig. 4A-C**). This interface in EFR3A is composed of the C-terminal region of the α2-helix, the N-terminal region of the α3-helix, and the residues between these two helices. This packs up against two α-helices in FAM126A (53-66 and 97-117).

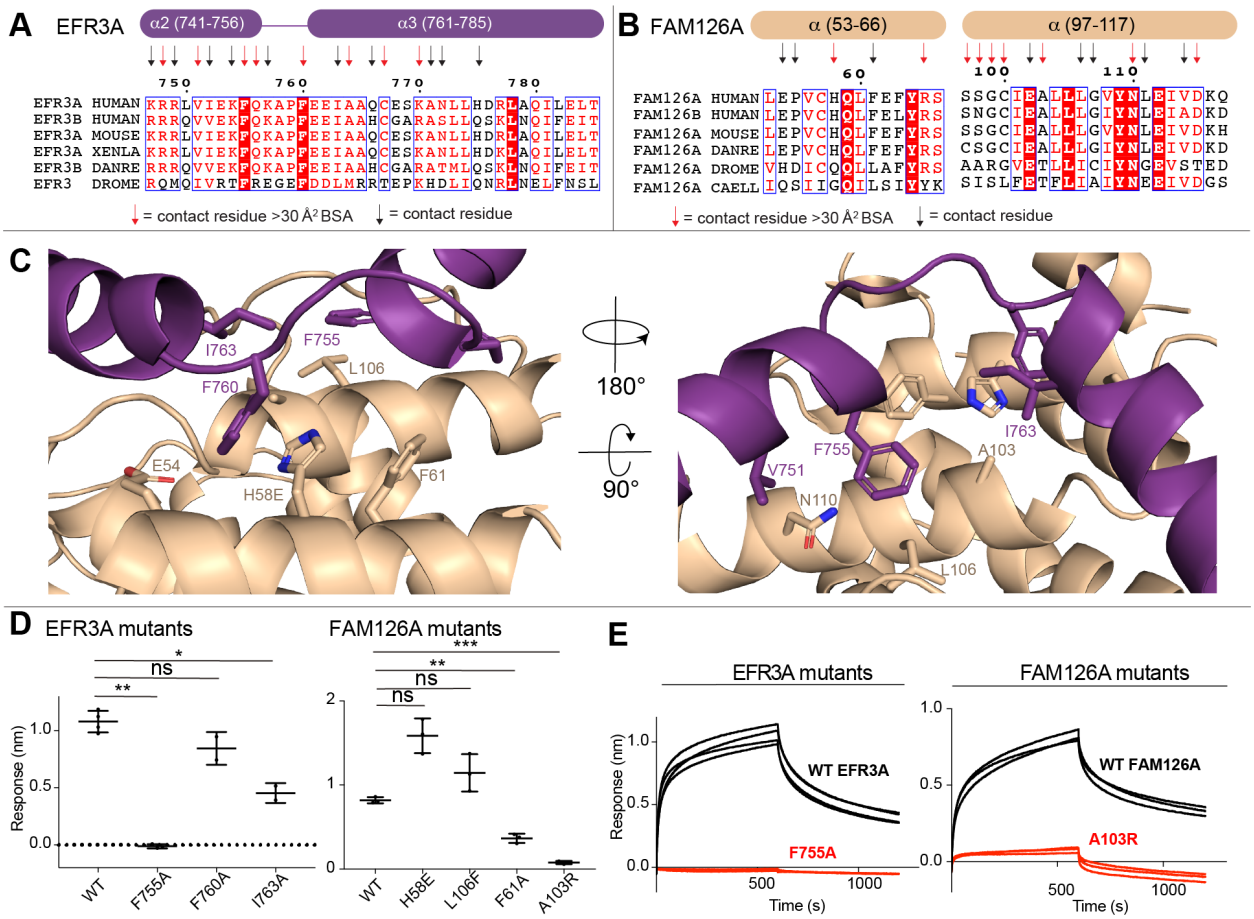


**Figure 4. Mutational analysis validates the EFR3A-FAM126A binding interface**

**A.** Multiple sequence alignment of EFR3A from *Homo sapiens, Mus musculus, Xenopus laevis, Danio rerio and Drosophila melanogaster*. EFR3A secondary structure of α2 and α3 helices are annotated above the alignment. Contact residues within 5 Å of FAM126A are annotated using arrows. Contact residues with BSA > 30 Å² are annotated using red arrows.

**B.** Multiple sequence alignment of FAM126A from *Homo sapiens, Mus musculus, Danio rerio, Drosophila melanogaster and Caenorhabditis elegans*. FAM126A secondary structure is annotated above the

292 alignment. Contact residues within 5 Å of EFR3A are annotated using arrows. Contact residues with BSA
293 > 30 $Å^2$ are annotated using red arrows.
294 **C.** Zoomed in cartoon view of the EFR3A-FAM126A interface with putative interfacial residues labelled.
295 EFR3A and FAM126A are coloured according to in-figure text.
296 **D.** Maximum BLI response of various EFR3A and FAM126A mutants compared to WT. Error is shown as
297 standard deviation (n=3) with p values indicated as follows: *p<0.01; **p<0.001; ***p<0.0001; not
298 significant (ns) > 0.01.
299 **E.** Raw BLI association and dissociation curves of EFR3A and FAM126A mutants compared to WT. His-
300 EFR3A was loaded on the anti-penta-His tip at 200 nM and dipped in TTC7B-FAM126A at 500 nM. Raw
301 BLI curves of all mutants in Supplemental Fig 5.
302
303 We generated several point mutations at the EFR3A-FAM126A interface and used
304 BLI to determine their effect on complex formation (**Fig 4D-E and Supplemental Fig 5**).
305 Mutation of residues F755A and I763A localized at the interface of helix α2 and α3 led to
306 decreased binding, with the F755A mutation causing the largest disruption. Mutation of
307 corresponding residues in FAM126A (F61A and A103R) also led to significant disruption
308 of EFR3A binding. This validates the previously unidentified critical role of FAM126A in
309 EFR3A binding, with this likely having important implications for PI4KA regulation.
310
311 *BRET analysis of EFR3-mediated plasma membrane recruitment*
312 To define the functional role of the identified interface between EFR3 and TTC7-
313 FAM126 in mediating PM localization of PI4KA, we developed a unique bioluminescence
314 resonance energy transfer (BRET) assay. These quantitative measurements utilized a
315 single-plasmid design containing a PM (Lyn Kinase N-Terminus; L10)-anchored BRET
316 acceptor (mVenus) and a nano-Luciferase (nLuc)-tagged PI4KA, which were separated
317 by a self-cleaving tandem viral 2A peptide sequence (tPT2A) to produce each protein in
318 transfected cells at a fixed stoichiometry (**Fig. 5A**). Upon addition of a cell-permeable
319 luciferase substrate (coelenterazine h; final concentration 5 μM), the signal from the nLuc-
320 generated luminescence and resulting mVenus fluorescence can be measured in entire
321 populations of live cells using a multimode microplate reader. Experiments were carried
322 out by transfecting this PM-PI4KA$^{BRET}$ biosensor (L10-mVenus-tPT2A-nLuc-PI4KA) along
323 with a single-plasmid encoding full length epitope-tagged EFR3B, TTC7B, and FAM126A

which also contains unique P2A and T2A splitting sequences between the specific components (EFR3B-P2A-TTC7B-T2A-FAM126A), as we have previously described (*31*).

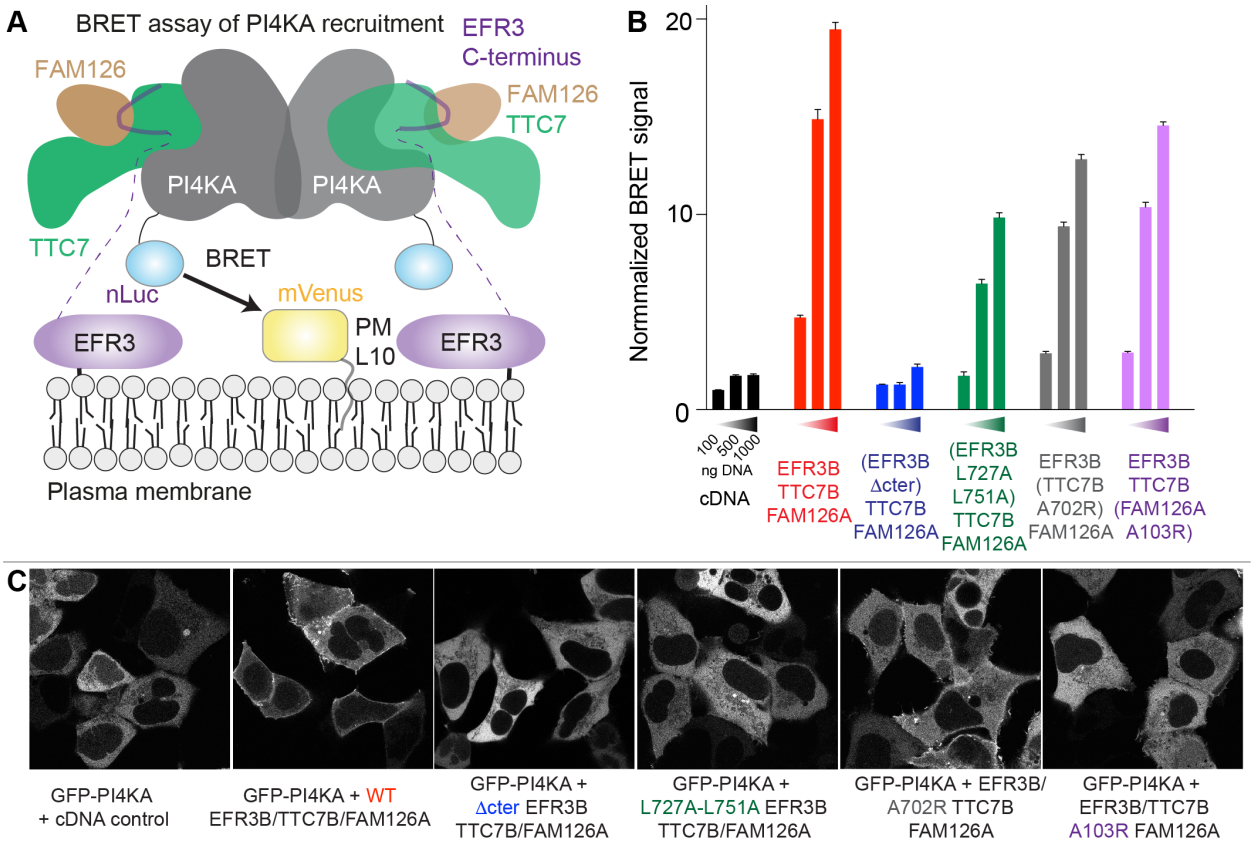


**Figure 5. The C-terminus of EFR3A mediates plasma membrane recruitment of PI4KA**

**A.** Cartoon depicting the quantitative BRET-based PI4KA recruitment assay. Briefly, the PM-anchored BRET acceptor (L10-mVenus) will only be near the nLuc-tagged PI4KA BRET-donor, and thereby efficiently increase the relative BRET signal, if co-assembled with the requisite molecular partners for PM targeting.

**B.** Normalized BRET signal measured from HEK293A cell populations (~0.75 x $10^5$ cells/well) expressing a fixed amount of the PM-PI4KA$^{BRET}$ biosensor (L10-mVenus-tPT2A-NLuc-PI4KA; 500 ng/ well) together with increasing amounts (100, 500, or 1000 ng/well) of constructs consisting of either an empty vector (black), wild-type control (red; EFR3B -P2A-TTC7B-T2A-FAM126A), or the indicated mutants of the PI4KA complex components (blue, EFR3B$^{\Delta cterm}$-P2A-TTC7B-T2A-FAM126A; green, EFR3B$^{L272A,L751A}$-P2A-TTC7B-T2A-FAM126A; grey, EFR3B-P2A-TTC7B$^{A702R}$-T2A-FAM126A; and, magenta, EFR3B-P2A-TTC7B-T2A-FAM126A$^{A103R}$). For all treatments, BRET values were normalized relative to an internal basal BRET control (PM-PI4KA$^{BRET}$ biosensor expressed without the empty

341 vector or EFR3B-P2A-TTC7B-T2A-FAM126A plasmid added) and are presented as the summary of
342 triplicate wells measured for each treatment condition in three independent biological replicates (n =
343 3, with normalized signals from 9 total wells averaged). Normalized BRET signals were then expressed
344 and graphed as fold-increases relative to the 100 ng/well pcDNA3.1 control.
345 **C.** Representative confocal images of live HEK293A cells co-expressing a fixed amount (250 ng) of
346 EGFP-PI4KA (greyscale) together with the indicated constructs (500 ng/each). The sequence and
347 colour-coding of the experimental treatments are matched with the BRET measurements in (**B**).
348
349 Live-cell experiments were carried out using HEK293A cells expressing a fixed
350 amount of the PM-PI4KA$^{BRET}$ biosensor (500ng/well), along with increasing amounts
351 (100, 500, and 1000 ng/well) of the EFR3B-TTC7B-FAM126A plasmid. Importantly, we
352 saw a clear dose-dependent increase in the basal BRET signal when full-length EFR3B,
353 TTC7B and FAM126A were co-expressed (red bars), consistent with an increase to the
354 PM recruitment of PI4KA (**Fig. 5B**). We then performed a control experiment where C-
355 terminus of EFR3B was truncated and saw no significant increase in the BRET signal
356 (blue bars) over an empty-vector control (black bars). Subsequently, we incorporated
357 complex disrupting mutations in EFR3B (L727A, L751A; green bars), TTC7B (A702R;
358 grey bars), and FAM126A (A103R; magenta bars), and saw a significantly reduced BRET
359 signal across the various levels of relative plasmid expression when compared to the wild-
360 type controls. However, all these mutants still had a measurable BRET signal above that
361 of the truncated EFR3B control (**Fig. 5B**). This indicates the importance of avidity in PI4KA
362 recruitment, as none of these mutations affecting the complex interface were able to
363 completely abrogate PI4KA localization to the PM. In parallel with this BRET-based
364 approach, we also used confocal microscopy for live-cell imaging studies to examine the
365 subcellular localization of an EGFP-tagged PI4KA construct after co-expression of
366 EFR3B, TTC7B, and FAM126A. Similar to our quantitative BRET-based measurements,
367 we only saw robust PM localization of EGFP-PI4KA when co-expressed together with the
368 wild-type EFR3B, TTC7B and FAM126A, and very limited PM localization of EGFP-PI4KA
369 in conjunction with the mutant or truncated versions of EFR3B, TTC7B, and FAM126A
370 (**Fig. 5C**).
371

372 **Discussion**

373 Understanding how PI4KA is recruited, activated, and regulated at the PM is
374 essential in developing therapeutic strategies for targeting human diseases associated
375 with loss-of-function of PI4KA. PI4KA, TTC7A and FAM126A mutations have been
376 identified in immunological, neurological, gastrointestinal, and developmental disorders
377 (*9–12*, *18*, *32*). Some cancers also require EFR3 and PI4KA activity for their aggressive
378 growth (*13*, *14*). Here, we report the architecture of the EFR3A complex that is formed
379 with PI4KA-TTC7B-FAM126A, revealing novel insights into the molecular mechanisms
380 underlying PM recruitment of PI4KA.

381 Our cryo-EM and HDX-MS analyses reveal that EFR3A forms an extended
382 interface with both the TTC7 and FAM126 regulatory proteins. Previous analysis of
383 evolutionarily conserved surfaces in TTC7 and FAM126 had led to the proposal of an
384 EFR3 interface composed of both proteins (*17*), and our work provides the first
385 experimental evidence of the cooperation between TTC7 and FAM126 for EFR3 binding.
386 This was validated by complex-disrupting mutations in EFR3A at both the FAM126A and
387 TTC7B interfaces, as well as mutations in FAM126A and TTC7B at the interface with
388 EFR3A. There was no difference in the conformation of PI4KA upon binding EFR3A in
389 solution, suggesting that there are no allosteric conformational changes upon EFR3A
390 binding. However, further biochemical and biophysical analysis of membrane resident
391 full-length EFR3 recruiting the PI4KA complex to membranes will be required to fully
392 understand the conformational dynamics of PI4KA upon membrane recruitment.

393 An important implication of this structure is that the two EFR3 isoforms may be
394 able to be selectively recruited to specific combinations of TTC7 and FAM126 isoforms.
395 While the binding interfaces are conserved in different isoforms, this conservation is not
396 absolute, allowing for the possibility of unique binding affinities. Isoforms of TTC7,
397 FAM126 and EFR3 are differentially expressed in diverse tissues, with many tissues
398 expressing multiple isoforms. The isoform-specific roles of the PI4KA regulatory proteins
399 are still not fully elucidated. The potential for unique molecular roles for the isoform-
400 specific PI4KA complexes has been recently highlighted for TTC7A and TTC7B, with
401 patients having disease-linked loss of function mutations in TTC7A in tissues that express

402 both TTC7A and TTC7B, where it appears that TTC7B cannot compensate for the loss
403 of TTC7A. This may be driven by differences in TTC7A/TTC7B expression during
404 embryogenesis, where TTC7A is widely expressed, and TTC7B is primarily expressed in
405 brain tissues (*33*). As the experimental structure of TTC7A is unknown, we examined
406 AlphaFold2 predicted models of TTC7A compared to our structure, with a focus on
407 potential differences at the EFR3A interface. Intriguingly, there is a weakly predicted
408 TTC7A helix (residues 678-690) in the same location as the α1 helix of EFR3A, with this
409 region being only weakly conserved in TTC7B (**Supplemental Fig 6A**) (*34*). In both
410 TTC7A and TTC7B there are multiple putative phosphorylated residues in this region (*35*),
411 which may alter the conformation of the EFR3 binding surface. Further analysis of
412 differences in EFR3 binding to TTC7A or TTC7B containing PI4KA complexes and how
413 phosphorylation of TTC7A/B alters EFR3 binding will be required to understand the
414 dynamic regulation of PI4KA membrane recruitment.

415 While subtle differences between complexes of TTC7A and TTC7B with the EFR3
416 C-terminus and FAM126 may exist, our structure of EFR3A bound to PI4KA-TTC7B-
417 FAM126A still allows for interrogation of the possible molecular mechanisms underlying
418 missense, nonsense and point mutations in TTC7A that cause severe gastrointestinal
419 and immunological disease. This disease is an autosomal-recessively inherited disease,
420 with patients having heterogeneous intestinal and immunologic disease presentations.
421 The most severe TTC7A mutations cause nonsense or frameshift mutations in TTC7A
422 that collectively remove both the EFR3 and PI4KA binding sites (*33*). However, there are
423 numerous missense mutations that cluster to regions in spatial proximity to the putative
424 EFR3 binding site in TTC7A. The mutations S539L, A551D, and H570R are all in helices
425 that either bind the α3 helix of EFR3A, or pack against the interfacial helices, with these
426 likely altering the orientation of the EFR3A binding site. In addition, K606R is predicted to
427 pack against the helix 704-724 in TTC7A (equivalent to the EFR3 interfacial helix 690-
428 707 in TTC7B). This mutation would likely alter the orientation of the EFR3 interface,
429 causing decreased affinity. Further biochemical and biophysical analysis will be required
430 to define the effect of disease-causing TTC7A mutations on EFR3-mediated membrane
431 recruitment versus PI4KA complex stability.

432 EFR3 proteins act as the membrane localization signal for the PI4KA complex (*5*),
433 with a palmitoylation code controlling their spatial organisation between liquid-ordered
434 and disordered regions of the PM (*22*). It has been previously revealed that there is an
435 aspect of plasticity in how EFR3 recruits PI4KA, as the integral membrane protein
436 TMEM150A can function in tandem with EFR3 to recruit PI4KA to the PM in the absence
437 of TTC7-FAM126 (*22*, *36*). Our structure reveals the canonical mechanism of PM
438 recruitment mediated by TTC7-FAM126. EFR3A mutations developed in this study that
439 only disrupt TTC7-FAM126-mediated recruitment may also act as unique tools to discern
440 between the diverse mechanisms of PI4KA recruitment to the PM. The triple helical
441 binding interface of EFR3 that binds to TTC7-FAM126 contains multiple phosphorylation
442 sites, present in both EFR3A and EFR3B (*35*). The location of these sites is divergent
443 between EFR3A and EFR3B, potentially suggesting differential regulation
444 (**Supplemental Fig 6B**). Further identification of the kinases and phosphatases that
445 target these sites will be required to fully understand how the EFR3 interface can be
446 regulated.
447 A limitation of the molecular insight we have observed for how EFR3 interacts with
448 the PI4KA complex is that all our biophysical observations on the association of the EFR3
449 C-terminus with the PI4KA complex were carried out exclusively in solution. The
450 biologically relevant association of EFR3 will occur in the context of the full length EFR3
451 localised on a membrane surface. While we have no expectation of the ordered domains
452 of EFR3 altering how the C-terminus binds to the PI4KA complex, there likely will be a
453 critical role of this region in proper EFR3 membrane localisation. For the evolutionarily
454 similar class I-III PI3Ks and PI4KB there are extensive conformational changes in the lipid
455 kinase domain that are driven by association with membrane substrate, and it is likely
456 that this will also be the case for PI4KA. To completely identify the full repertoire of
457 regulatory mechanisms underlying PI4KA activation future experiments will need to
458 address conformational dynamics of full-length lipidated EFR3 recruitment of the PI4KA
459 complex in its native membrane environment.
460 Collectively, our detailed biochemical and structural analyses of the EFR3A-
461 mediated recruitment of PI4KA complex to the PM provides unique insight into the

assembly and regulation of PI4KA complexes. This work also provides a framework to further explore how PM recruitment of PI4KA is regulated. Overall, the findings from this study will be useful in developing novel therapeutic strategies to target aberrant PI4KA signaling in human disease.

**Acknowledgements**

JEB is supported by the Natural Science and Engineering Research council (Discovery grant NSERC-2020-04241), and a Michael Smith Foundation for Health Research (Scholar Award 17686). ALS was supported by an NSERC CGS-M scholarship. C.K.Y. is supported by CIHR (PJT-168907) and the Natural Sciences and Engineering Research Council of Canada (RGPIN-2018-03951). Cryo-EM specimens were prepared, and data was collected at the High-Resolution Macromolecular Electron Microscopy (HRMEM) facility at the University of British Columbia (https://cryoem.med.ubc.ca). We thank Claire Atkinson, Joeseph Felt, Liam Worrall and Natalie Strynadka. HRMEM is funded by the Canadian Foundation for Innovation and the British Columbia Knowledge Development Fund. The work of TB, JGP, PR and AAP was funded by the Intramural Research Program of the *Eunice Kennedy Shriver* National Institute of Child Health and Human Development of the National Institutes of Health, Bethesda, MD, USA. (HHS/NIH/NICHD - Z01:HD000196-25). Confocal imaging was performed at the Microscopy & Imaging Core of the NICHD with the kind assistance of Drs. Vincent Schram and Ling Yi.

**Competing Interests**

J.E.B. reports personal fees from Scorpion Therapeutics and Reactive therapeutics; and research contracts from Novartis and Calico Life Sciences.

**Data Availability**

The EM data have been deposited in the EM data bank with accession number (EMDB: 44413), and the associated structural model has been deposited to the PDB with accession number (PDB: 9BAX). The MS proteomics data have been deposited to the

492 ProteomeXchange Consortium via the PRIDE partner repository with the dataset identifier
493 PXD043442 (*37*). All raw data in all figures are available in the source data excel file.
494
495 **Methods**
496 ***Plasmid constructs***
497 Plasmids containing genes for full length PI4KA, TTC7B and FAM126A (1-308) were
498 cloned into the MultiBac vector, pACEBac1 (Geneva Biotech) as described in (*20*).
499 Plasmid encoding TTC7B and FAM126A (1-308) was subcloned into a vector containing
500 an N-terminal 10X histidine tag, followed by a 2X Strep tag, followed by a Tobacco Etch
501 Virus (TEV) protease cleavage site. Based on the evolutionary conservation of the C-
502 terminal tail of EFR3A (**Fig. S1**), we designed and synthesized a construct containing the
503 C-terminus of EFR3A from residue 688 to 821 from GeneArt gene synthesis (Invitrogen).
504 EFR3A (721-791) was subcloned into two vectors; one containing an N-terminal 10X
505 histidine tag and a 2X Strep tag, and one containing an N terminal Maltose Binding Protein
506 (MBP) tag in addition to the 10X Histidine tag and 2X Strep tag (*38*). EFR3A, TTC7B and
507 FAM126A substitution mutants shown in Table S2 were generated using site-directed
508 mutagenesis according to published protocols using EFR3A (721-791) as template.
509 Plasmid encoding human EFR3B$^{HA}$-T2A-TTCB$^{MYC}$-P2A-$^{FLAG}$FAM126A in pcDNA3.1
510 vector, which is referred to more simply here as EFR3B-P2A-TTC7B-T2A-FAM126A was
511 a kind gift from the Cyert lab at Stanford university. EFR3B, TTC7B and FAM126A
512 substitution and deletion mutants shown in Table S2 in the pcDNA3.1 vector were
513 generated using Gibson assembly (*38*).
514 Alternatively, the high-sensitivity PM-PI4KA$^{BRET}$ biosensor (L10-mVenus-tPT2A-
515 nLuc-PI4KA) was constructed in multiple steps by standard restriction cloning using
516 enzymes from New England Biolabs. First, the sLuc cassette in the L10-mVenus-T2A-
517 sLuc-(2X)P4M biosensor (*39*) was exchanged for NanoLuciferase (nLuc) using an insert
518 amplified from PM-nLuc (Forward Primer, 5'- AT ATA CCG GTC ATG GTC TTC ACA
519 CTC GAA GAT TTC GTT GG -3'; Reverse Primer, 5'- AT ATC TCG AGA CGC CAG AAT
520 GCG TTC GCA CAG C -3'), which was a kind gift from Laszlo Hunyady (Addgene Plasmid
521 # 164784), together with AgeI and XhoI restriction sites. Next, we replaced the single T2A

522 site in the resulting L10-mVenus-T2A-nLuc-(2X)P4M biosensor with the tandem tPT2A
523 sequence (*40*) using a custom-synthesized insert from GeneArt (Invitrogen) and a SalI
524 and AgeI double-digest. Finally, we replaced the (2X)P4M domain in the L10-mVenus-
525 tPT2A-nLuc-(2X)P4M vector with an in-frame PI4KA insert derived from pEGFP-PI4KA
526 (*41*) using shared XhoI and MfeI restriction sites in the parent C1 vector backbones
527 (CloneTech). Whole plasmid sequencing for all plasmids was performed by
528 Plasmidsaurus using Oxford Nanopore Technology with custom analysis and annotation.
529
530 ***Protein Expression***
531 Plasmids containing the coding sequences for EFR3A (721-791), were expressed in BL21
532 DE3 C41 *Escherichia coli* and induced with 0.5 mM IPTG and grown at 37 °C for 4 h. The
533 TTC7B-FAM126A (1-308) construct was expressed in BL21 DE3 C41 cells and induced
534 with 0.1mM IPTG and grown at 21 °C for 20 hours. Cells were then harvested and
535 centrifuged at 15,000*g*. Pellets were washed with PBS before being snap-frozen in liquid
536 nitrogen, followed by storage at –80 °C. Bacmid harboring PI4KA complex (PI4KA-
537 TTC7B-FAM126A (1-308)) was transfected into *Spodoptera frugiperda (Sf9) cells*, and
538 viral stocks amplified for one generation to acquire a P2 generation final viral stock. Final
539 viral stocks were added to *Sf9* cells in a 1/100 virus volume to cell volume ratio.
540 Constructs were expressed for 65-72 hours before harvesting of the infected cells. Cell
541 pellets were washed with PBS before being snap-frozen in liquid nitrogen, followed by
542 storage at –80 °C.
543
544 ***Protein Purification***
545 *EFR3A purification:* Cell pellets were lysed by sonication for 5 min in lysis buffer (20 mM
546 Tris [pH 8.0], 100 mM NaCl, 5% [v/v] glycerol, 20 mM imidazole, 2 mM β-
547 mercaptoethanol [bME]), and protease inhibitors [Millipore Protease Inhibitor Cocktail Set
548 III, EDTA free]). Triton X-100 was added to 0.1% v/v, and the solution was centrifuged for
549 45 min at 20,000*g* at 1 °C (Beckman Coulter J2-21, JA-20 rotor). The supernatant was
550 then loaded onto a 5 ml HisTrap column (Cytiva) that had been equilibrated in nickel–
551 nitrilotriacetic acid (Ni–NTA) A buffer (20 mM Tris [pH 8.0], 100 mM NaCl, 20 mM

552 imidazole [pH 8.0], 5% [v/v] glycerol, and 2 mM bME). The column was washed with of
553 high salt buffer (20 mM Tris [pH 8.0], 1 M NaCl, 5% [v/v] glycerol, and 2 mM bME),
554 followed by of 6% Ni–NTA B buffer (20 mM Tris [pH 8.0], 100 mM NaCl, 200 mM
555 imidazole [pH 8.0], 5% [v/v] glycerol, and 2 mM bME) before being eluted with 100% Ni–
556 NTA B. The eluate was then loaded onto a 5 ml Strep column and then washed with GFB
557 (20 mM HEPES [pH 7.5], 150 mM NaCl, 5% [v/v] glycerol and 1 mM Tris(2-carboxyethyl)
558 phosphine [TCEP]). Protein was eluted with GFB containing 2.5 mM desthiobiotin and
559 concentrated in a 10 kDa MWCO concentrator (Millipore Sigma). Concentrated protein
560 was loaded onto the Superdex 75 Increase 10/300 GL (Cytiva) pre-equilibrated in GFB.
561 Protein fractions were collected and concentrated in a 10 kDa MWCO concentrator
562 (Millipore Sigma), flash frozen in liquid nitrogen and stored at –80 °C.

563 *TTC7B-FAM126A (1-308) purification:* Cell pellets were lysed by sonication for
564 5 min in lysis buffer (20 mM imidazole [pH 8.0], 100 mM NaCl, 5% [v/v] glycerol, 2 mM
565 bME), and protease inhibitors [Millipore Protease Inhibitor Cocktail Set III, animal-free].
566 Triton X-100 was added to 0.1% v/v, and the solution was centrifuged for 45 min at
567 20,000*g* at 1 °C. The supernatant was then loaded onto a 5 ml HisTrap column (Cytiva)
568 that had been equilibrated in nickel–nitrilotriacetic acid (Ni–NTA) A buffer (20 mM Tris [pH
569 8.0], 100 mM NaCl, 20 mM imidazole [pH 8.0], 5% [v/v] glycerol, and 2 mM bME). The
570 column was washed with Ni-NTA A buffer (20 mM imidazole [pH 8.0], 100 mM NaCl, 5%
571 [v/v] glycerol, and 2 mM bME) followed by 6% Ni–NTA B buffer (450 mM Imidazole [pH
572 8.0], 100 mM NaCl, 5% [v/v] glycerol, and 2 mM bME) before being eluted with 100% Ni–
573 NTA B. The eluate was then loaded onto a 5 ml Strep column and then washed with
574 filtration buffer (GFB) (20 mM Imidazole [pH 7.0], 150 mM NaCl, 5% [v/v] glycerol and
575 0.5 mM Tris(2-carboxyethyl) phosphine (TCEP)). The column was loaded with tobacco
576 etch virus protease containing a stabilizing lipoyl domain. TEV cleavage proceeded
577 overnight following which the protein was eluted with GFB. Protein eluate was further
578 concentrated in a 50 kDa MWCO concentrator (Millipore Sigma). Concentrated protein
579 was loaded onto the Superose 6 Increase 10/300 GL (Cytiva) pre-equilibrated in GFB.
580 Protein fractions from a single peak were collected and concentrated in 50 kDa MWCO

581 concentrator (Millipore Sigma), flash frozen in liquid nitrogen and stored at -80 °C until
582 further use. This protein is referred to as TTC7B/FAM126A.
583 *PI4KA-TTC7B-FAM126A (1-308) purification*: Sf9 pellets were resuspended in
584 lysis buffer [20 mM imidazole pH 8.0, 100 mM NaCl, 5% glycerol, 2 mM βMe, protease
585 (Protease Inhibitor Cocktail Set III, Sigma)] and lysed by sonication. Triton X-100 was
586 added to 0.1% v/v final, and lysate was centrifuged for 45 min at 20,000×g at 1 °C. The
587 supernatant was then loaded onto a 5 ml HisTrap column (Cytiva) that had been
588 equilibrated in nickel–nitrilotriacetic acid (Ni–NTA) A buffer (20 mM Tris [pH 8.0], 100 mM
589 NaCl, 20 mM imidazole [pH 8.0], 5% [v/v] glycerol, and 2 mM bME). The column was
590 washed with Ni-NTA A buffer (20 mM imidazole [pH 8.0], 100 mM NaCl, 5% [v/v] glycerol,
591 and 2 mM bME) followed by 6% Ni–NTA B buffer (27 mM Imidazole [pH 8.0], 100 mM
592 NaCl, 5% [v/v] glycerol, and 2 mM bME) before being eluted with 100% Ni–NTA B. Elution
593 fractions were passed through a 5 ml StrepTrapHP column (Cytiva) pre-equilibrated in
594 Gel Filtration buffer (GFB) (20 mM imidazole pH 7.0, 150 mM NaCl, 5% glycerol [v/v], 0.5
595 mM TCEP). The column was washed with GFB before loading a tobacco etch virus
596 protease containing a stabilizing lipoyl domain (Lip-TEV), and cleavage proceeded
597 overnight. Cleaved protein was eluted with GFB and concentrated in a 50 kDa MWCO
598 concentrator (MilliporeSigma). Concentrated protein was loaded onto the Superose 6
599 Increase 10/300 GL (Cytiva) pre-equilibrated in GFB. Protein fractions from a single peak
600 were collected and concentrated in 50 kDa MWCO concentrator (Millipore Sigma), flash-
601 frozen in liquid nitrogen and stored at -80 °C until further use. This protein is referred to
602 as PI4KA complex.
603
604 ***Co-elution of PI4KA complex-EFR3A and TTC7B-FAM126A (1-308)-EFR3A***
605 7.19 μM of PI4KA complex and 61.8 μM of EFR3A were loaded onto a Superose 6
606 Increase column pre-equilibrated in GFB [150 mM NaCl, 20 mM imidazole (pH 7.0), 5%
607 glycerol (v/v), 0.5 mM TCEP]. Fractions containing the PI4KA complex bound to EFR3A
608 were pooled, concentrated, flash-frozen in liquid nitrogen and stored at -80°C. Protein
609 was run on an SDS-PAGE gel to confirm the formation of the complex. For the co-elution
610 of TTC7B-FAM126A (1-308) and EFR3A, we used 6.78 μM of TTC7B-FAM126A and

611 102.3 µM of EFR3A and performed size exclusion chromatography as mentioned above.
612 Fresh protein was run on an SDS-PAGE gel to confirm formation of complex.
613
614 ***Protein purification for Cryo-EM***
615 Pre-Gel filtered PI4KA complex (13.0 µM final), and gel filtered EFR3A (113 µM final)
616 were incubated together on ice for 20 minutes prior to injection onto the Superose 6
617 Increase 10/300 GL (Cytiva) pre-equilibrated in GFB (150 mM NaCl, 20 mM imidazole
618 [pH 7.0], 5% glycerol [v/v], 0.5 mM TCEP). Protein fractions from a single peak were
619 collected and concentrated to 250 µl at 4µM and BS3 was added to a final concentration
620 of 1 mM. The reaction was incubated on ice for 1 hour. 1 M Tris (pH 7.5) was added to a
621 final concentration of 50 mM to quench the reaction and incubated at RT for 15 minutes.
622 The quenched reaction was loaded onto the Superose 6 Increase 10/300 column pre-
623 equilibrated in GFB. Protein fractions from the main peak, consistent with an elution
624 volume of the PI4KA complex-EFR3A (721-791), were collected, concentrated, flash
625 frozen in liquid nitrogen, and stored at -80$^{o}$C.
626
627 ***Cryo-EM sample preparation and data collection***
628 C-Flat 2/1-3Cu-T-50 grids mesh grids were glow-discharged for 25 s at 15 mA using a
629 Pelco easiGlow glow discharger. 3 µL of crosslinked PI4KA complex-EFR3A (721-791)
630 were applied to the grids at 0.7 mg/ml. The grids were prepared using a Vitrobot Mark IV
631 (FEI) by blotting for 1.5 seconds at a blot force of -5 at 4°C and 100% humidity before
632 plunge freezing in liquid ethane. Grids were screened for particle and ice quality at the
633 UBC High Resolution Macromolecular Cryo-Electron Microscopy (HRMEM) facility using
634 a 200-kV Glacios transmission microscope (Thermo Fisher Scientific) equipped with a
635 Falcon 3EC direct electron detector (DED). Datasets were collected at the UBC HRMEM
636 facility using a 300-kV Titan Krios equipped with Selectris energy filter with a Falcon IV
637 camera. A total of 9,412 super-resolution movies were collected using SerialEM with a
638 total dose of 50 $e^{-}$/Å$^{2}$ over 774 frames at a physical pixel size of 0.77 Å per pixel, using a
639 defocus range of -0.5 to -2 um, at 165,000 x magnification.
640

641 ***Cryo-EM image processing***

642 All data processing was carried out with cryoSPARC v4.2.1. Patch motion correction
643 using default settings was applied to all movies to align the frames and Fourier-crop the
644 outputs by a factor of 2. The contrast transfer function (CTF) of the resulting micrographs
645 was estimated using the patch CTF estimation job with default settings. Micrographs were
646 manually curated to contain micrographs with CTF fit resolution less than or equal to 10.

647 To generate an initial model, 277,573 particles were picked from 3,501
648 micrographs using blob picking with a minimum and maximum diameter of 250 and 280,
649 respectively. Particles were inspected using the inspect picks job to remove particles that
650 picked ice contamination and were then extracted with a box size of 500 pixels, for a total
651 of 201,081 particles. The particles were subjected to 2D classification using default
652 settings. The best class averages were then selected and used as an initial model for
653 template picking. These 2D classes were low pass filtered to 20 Å and used to template
654 pick with the particle diameter set to 300 Å. Particles were inspected and 510,887 were
655 extracted with a box size of 600 pixels and subjected to two rounds of 2D classification
656 with 40 online-EM iterations to remove particles with ice contamination or those that
657 showed no features. A total of 77,624 particles were used for ab initio reconstruction and
658 heterogeneous refinement using three classes, with C1 symmetry. Given the previously
659 solved PI4KA/TTC7B/FAM126A (2-289) cryo-EM structure employing C2 symmetry (*17*),
660 the following homogenous refinements were done with C2 symmetry. The best
661 heterogeneous refinement which had 46,039 particles underwent two rounds of
662 homogenous refinement. These 46,039 particles were subjected to further ab initio 3D
663 reconstructions, heterogeneous refinement, and homogeneous refinement jobs to filter
664 out incorrectly assigned particles. The final initial model to be used to generate templates
665 for auto-picking of particles consisted of 8,647 particles.

666 To generate a cryo-EM map from the complete dataset, the collected movies were
667 split into three groups (Group 1: 3,535 movies, Group 2: 3,364 movies, Group 3: 2,513
668 movies) and processed into micrographs as described above. The initial template from
669 above was used to auto-pick 493,392 (group 1), 415,293 (group 2), and 307,632 (group
670 3) particles, using the template picker job with particle diameter set to 300 Å and a

671 minimum separation distance of 0.75 diameters. Particles were inspected as above and
672 275,667 (group 1), 264,196 (group 2), and 185,766 (group 3) particles were extracted
673 with a box size of 600 pixels. Each group of particles independently underwent one (group
674 1) or two (groups 2 and 3) rounds of 2D classification with 40 online-EM iterations. The
675 resulting 105,657 (group 1), 57,805 (group 2), and 77,900 (group 3) particles were
676 independently used for ab initio reconstruction using 3 classes and subsequent
677 heterogeneous refinement with C1 symmetry. The best 3D classification from groups 1
678 and 2 were merged into 93,029 particles (55,802 (group 1) + 37,227 (group 2)) and
679 underwent two rounds of ab initio reconstruction with 3 classes followed by heterogenous
680 refinement. The best 3D classification, consisting of 44,305 particles was refined using
681 homogeneous refinement using C1 symmetry. The particles from group 3 were then
682 added to these 44,305 particles. A total of 67,563 particles were used to carry out
683 homogeneous refinement using the previous 3D reconstruction as the starting model,
684 yielding a reconstruction with an overall resolution of 3.63 Å based on the Fourier shell
685 correlation (FSC) 0.143 criterion. The full workflow to generate the final cryo-EM map
686 from the three groups is shown in **Supplemental Fig 2**.
687
688 ***Model building***
689 The cryo-EM structure of PI4KA-TTC7B-FAM126A (PDB: 6BQ1) (*17*) was fit into the map
690 using Chimera(*42*). The 1st helix of EFR3A was at sufficient local resolution for iterative
691 rounds of automated model building in Phenix, manual model building in COOT, and
692 refinement in Phenix.real_space_refine using realspace, rigid body, and adp refinement
693 with tight secondary structure restraints (*43*). For the remainder of the EFR3A interface
694 with FAM126A and TTC7B we utilized AlphaFold-Multimer using Google Colab
695 (*27*)(https://colab.research.google.com/github/sokrypton/ColabFold/blob/main/AlphaFold
696 2.ipynb) was used to model the structure of TTC7B-FAM126A–EFR3A. The sequences
697 of full length TTC7B, residues 1-360 of FAM126A with residues 681-821 of EFR3A were
698 input to generate the model of the complex. AlphaFold generated five models ranked in
699 order by mean pLDDT. The highest ranked model showed strong correlation to the cryo-
700 EM density, and was used to model the 2nd and 3rd helix of EFR3A bound to FAM126A

701 and TTC7B, with multiple rounds of refinement in Phenix.real_space_refine using
702 realspace, rigid body, and adp refinement with tight secondary structure restraints (*43*).
703 The full refinement and validation statistics are shown in **Supplementary Table 1**.
704
705 ***HDX-MS sample preparation***
706 HDX reactions examining the TTC7B-FAM126A (1-308) in the presence and absence of
707 EFR3A were carried out in 15 $\mu$L reaction volumes containing 15 pmol of protein (1 $\mu$M
708 TTC7B-FAM126A, 1 $\mu$M EFR3A in the bound state). The exchange reactions were
709 initiated by the addition of 12.55 $\mu$L of $D_2O$ buffer (20 mM Imidazole pH 7, 150 mM NaCl)
710 to 2.45 $\mu$L of protein (final $D_2O$ concentration of 78.2% [v/v]). Reactions proceeded for 3s,
711 30s, 300s, 3000s, and 10,000s at 20°C before being quenched with ice cold acidic quench
712 buffer, resulting in a final concentration of 0.6M guanidine HCl and 0.9% formic acid.
713 HDX reactions examining the PI4KA complex in the presence and absence of
714 EFR3A were carried out in 15 $\mu$L reaction volumes containing 10 pmol of protein (0.667
715 $\mu$M PI4KA complex, 0.667 $\mu$M EFR3A in the bound state). The exchange reactions were
716 initiated by the addition of 10.92 $\mu$L of $D_2O$ buffer (20 mM Imidazole pH 7, 150 mM NaCl)
717 to 4.08 $\mu$L of protein (final $D_2O$ concentration of 68.0 % [v/v]). Reactions proceeded for
718 30s, 300s, 3000s, and 10,000s at 20°C before being quenched with ice cold acidic quench
719 buffer, resulting in a final concentration of 0.6M guanidine HCl and 0.9% formic acid post
720 quench.
721 HDX reactions examining MBP-EFR3A in the presence and absence of the
722 TTC7B-FAM126A (1-308) were carried out in 20 $\mu$L reaction volumes containing 25 pmol
723 of protein (1.25 $\mu$M MBP-EFR3A, 1.25 $\mu$M TTC7B-FAM126A in the bound state). The
724 exchange reactions were initiated by the addition of 14.66 $\mu$L of $D_2O$ buffer (20 mM
725 Imidazole pH 7, 150 mM NaCl) to 5.34 $\mu$L of protein (final $D_2O$ concentration of 68.5 %
726 [v/v]). Reactions proceeded for 3s, 30s, and 300s at 20°C and 0.3s (3s on ice) before
727 being quenched with ice cold acidic quench buffer, resulting in a final concentration of
728 0.6M guanidine HCl and 0.9% formic acid post quench.
729 All conditions and timepoints were created and run in independent triplicate. All
730 samples were flash frozen immediately after quenching and stored at -80°C.

731

732 ***Protein digestion and MS/MS data collection***

733 Protein samples were rapidly thawed and injected onto an integrated fluidics system
734 containing a HDx-3 PAL liquid handling robot and climate-controlled (2°C)
735 chromatography system (Trajan), a Dionex Ultimate 3000 UHPLC system, as well as an
736 Impact HD QTOF Mass spectrometer (Bruker). The full details of the automated LC
737 system are described in (*44*). The TTC7B-FAM126A and PI4KA complex samples were
738 run over one immobilized pepsin column (Trajan; ProDx protease column, 2.1 mm x 30
739 mm PDX.PP01-F32) at 200 *µ*L/min for 3 minutes at 10°C, and the MBP-EFR3A samples
740 were run over two immobilized pepsin columns (Waters; Enzymate Protein Pepsin
741 Column, 300Å, 5*µ*m, 2.1 mm X 30 mm) at 350 *µ*L/min for 3 minutes at 2°C. The resulting
742 peptides were collected and desalted on a C18 trap column (Acquity UPLC BEH C18
743 1.7mm column (2.1 mm x 5 mm); Waters 186004629). The trap was subsequently eluted
744 in line with an ACQUITY 1.7 µm particle, 100 mm × 2.1 mm C18 UPLC column (Waters;
745 186003686), using a gradient of 3-35% B (Buffer A 0.1% formic acid; Buffer B 100%
746 acetonitrile) over 11 minutes immediately followed by a gradient of 35-80% over 5
747 minutes. Mass spectrometry experiments acquired over a mass range from 150 to 2200
748 m/z using an electrospray ionization source operated at a temperature of 200°C and a
749 spray voltage of 4.5 kV.

750

751 ***Peptide identification***

752 Peptides were identified from non-deuterated samples using data-dependent acquisition
753 following tandem MS/MS experiments (0.5s precursor scan from 150-2000 m/z; twelve
754 0.25s fragment scans from 150-2000 m/z). TTC7B-FAM126A (1-308) and PI4KA complex
755 MS/MS datasets were analysed using PEAKS7 (PEAKS), and peptide identification was
756 carried out using a false discovery-based approach, with a threshold set to 1% using a
757 database of purified proteins and known contaminants (*45*). The search parameters were
758 set with a precursor tolerance of 20 ppm, fragment mass error 0.02 Da charge states from
759 1-8, leading to a selection criterion of peptides that had a -10logP score of 25.2 and 20.4
760 respectively. MBP-EFR3A (721-791) MS/MS datasets were analysed using FragPipe

761 v18.0 and peptide identification was carried out by using a false discovery-based
762 approach using a database of purified proteins and known contaminants (*45*, *46*).
763 MSFragger was utilized, and the precursor mass tolerance error was set to -20 to 20ppm.
764 The fragment mass tolerance was set at 20ppm. Protein digestion was set as nonspecific,
765 searching between lengths of 4 and 50 aa, with a mass range of 400 to 5000 Da.
766
767 ***Mass Analysis of Peptide Centroids and Measurement of Deuterium Incorporation***
768 HD-Examiner Software (Sierra Analytics) was used to automatically calculate the level of
769 deuterium incorporation into each peptide. All peptides were manually inspected for
770 correct charge state, correct retention time, appropriate selection of isotopic distribution,
771 etc. Deuteration levels were calculated using the centroid of the experimental isotope
772 clusters. Results are presented as relative levels of deuterium incorporation, and the only
773 control for back exchange was the level of deuterium present in the buffer (78.2%, 68.0%,
774 or 68.5%). Differences in exchange in a peptide were considered significant if they met
775 all three of the following criteria: ≥5% change in exchange, ≥0.45 Da difference in
776 exchange, and a p value <0.01 using a two tailed student t-test. The entire HDX-MS
777 dataset with all the values and statistics are provided in the source data. Samples were
778 only compared within a single experiment and were never compared to experiments
779 completed at a different time with a different final $D_2O$ level. The data analysis statistics
780 for all HDX-MS experiments are provided in the source data according to the guidelines
781 of (*30*). HDX-MS proteomics data generated in this study have been deposited to the
782 ProteomeXchange Consortium via the PRIDE partner repository with the dataset identifier
783 PXD043442 (*37*).
784
785 ***Bio-layer interferometry (BLI)***
786 The BLI measurements were conducted using a Fortebio (Sartorius) K2 Octet using fiber
787 optic biosensors. Anti–penta-His biosensors were loaded using purified EFR3A, which
788 had a 10x His tag on the N-terminus. The biosensor tips were preincubated in the BLI
789 buffer (20 mM HEPES [pH 7.5], 150 mM NaCl, 0.01%, bovine serum albumin, and
790 0.002% Tween-20) for 10 min before experiments began. The sequence of steps in each

791 assay was regeneration, custom, loading, baseline, association, and dissociation. Every
792 experiment was done at 25 °C with shaking at 1000 rpm. Technical replicates were
793 performed by using the same fiber tip and repeating the steps outlined previously.
794 Regeneration was performed by exposing the tips to regeneration buffer (Glycine pH 1.5)
795 for 5s and BLI buffer for 5s and repeating the exposure for 6 cycles. BLI buffer was used
796 for the custom, baseline, and dissociation steps; these steps were performed in the same
797 well for a given sample. For the dose response in **Figure 3A**, EFR3A was diluted in BLI
798 buffer to 200 nM and was loaded onto the anti penta-His biosensor tips. TTC7B-
799 FAM126A was also diluted in BLI buffer from 2500 nM to 10 nM and added to the
800 appropriate association wells. For the mutant binding experiments, TTC7B-FAM126A
801 was diluted in BLI buffer to 500nM. All BLI experiments were performed using two or three
802 technical replicates. Means ± SD were used to present values. Statistical analysis
803 between conditions was performed using an unpaired t-test assuming unequal variances
804 analyzing mutant responses to wildtype responses measured simultaneously during each
805 assay. The concentration of a given mutant was compared with the same concentration
806 for wild-type binding. The following legends are used for statistical significance: ***
807 $p<0.0001$, **$p<0.001$, *$p< 0.01$ and ns $p>0.01$.
808

809 ***Multiple Sequence Alignments***

810 Sequences were aligned using Clustal Omega Multiple Sequence Alignment, and the
811 aligned sequences were subsequently analyzed by ESPript 3.0 (https://espript.ibcp.fr) to
812 visualize conserved regions (*47*). The UniProt accession codes for the aligned sequences
813 used for TTC7 in **Figure 3C** are Q86TV6 *(Homo sapiens)*, Q9ULT0 *(Homo sapiens)*,
814 E9Q6P5 *(Mus musculus)*, A0A8J1LRC8 *(Xenopus laevis)*, A0A8M2B4X5 *(Danio rerio),*
815 A0A0B4K7H0 *(Drosophila melanogaster)*. The UniProt accession codes for the aligned
816 sequences used for FAM126 in **Figure 4B** are Q9BYI3 *(Homo Sapiens)*, Q8IXS8 *(Homo*
817 *Sapiens)*, Q6P9N1 *(Mus musculus)*, Q6P121 *(Danio rerio)*, Q7K1C5 *(Drosophila*
818 *melanogaster)*, Q6A586 *(Caenorhabditis elegans)*. The UniProt accession codes for the
819 aligned sequences used for EFR3 in **Figures 3B, 4A and Supplemental Figure 1** are
820 Q14156 *(Homo Sapiens)*, Q9Y2G0 *(Homo sapiens)*, Q8BG67 *(Mus musculus)*, Q641A2

821 *(Xenopus laevis)*, Q5SPP5 *(Danio rerio)*, Q8IGJ0 *(Drosophila melanogaster)*, Q09263
822 *(Caenorhabditis elegans)*, O59817 *(Schizosaccharomyces pombe)*, Q03653
823 *(Saccharomyces cerevisiae)*.
824
825 ***Mammalian Cell Culture***
826 HEK293A (Invitrogen) cells were cultured in Dulbecco's Modified Eagle Medium (DMEM-
827 high glucose; Gibco) containing 10% (vol/vol) FBS and supplemented with a 1% solution
828 of penicillin/streptomycin (Gibco). Cells were maintained at 37°C and 5% $CO_2$ in a
829 humidified atmosphere and regularly tested for *Mycoplasma* contamination using a
830 commercially available detection kit (InvivoGen). After thawing, cell cultures are also
831 treated with plasmocin (InvivoGen) at 500 *μ*g/mL for the initial three passages (6-9 days)
832 as well as supplemented with 5 *μ*g/mL of the prophylactic for all subsequent passages.
833
834 ***Live-Cell Measurements using the PM-PI4KA$^{BRET}$ Biosensor***
835 HEK293A cells (0.75x$10^5$ cells/well) were seeded in a 200 µL total volume to white-bottom
836 96 well plates pre-coated with 0.01% poly-L-lysine solution (Sigma) and cultured
837 overnight. Cells were then transfected with 0.5 µg of the PM-PI4KA$^{BRET}$ biosensor (L10-
838 mVenus-tPT2A-nLuc-PI4KA) using Lipofectamine 2000 (1 µL/well). Lipofection was done
839 within Opti-MEM (40 µL/well) according to the manufacturer's protocol, but with the slight
840 modification of removing the media containing the Lipofectamine-complexed DNA and
841 replacing it with complete culture medium at between 4-6 hrs post-transfection. Where
842 indicated, increasing amounts (100, 500, or 1000 ng/well) of specified plasmids consisting
843 of either an empty vector (pcDNA3.1), wild-type positive control (EFR3B-P2A-TTC7B-
844 T2A-FAM126A), or the indicated mutants of the PI4KA complex components (EFR3B$^{\Delta}$
845 $^{cterm}$-P2A-TTC7B-T2A-FAM126A, EFR3B$^{L272A,L751A}$-P2A-TTC7B-T2A-FAM126A, EFR3B-
846 P2A-TTC7B$^{A702R}$-T2A-FAM126A, or EFR3B-P2A-TTC7B-T2A-FAM126A$^{A103R}$) were co-
847 transfected (0.5-1.5 µg/well total). BRET measurements were made at 37°C using a
848 Tristar2 LB 942 Multimode Microplate Reader (Berthold Technologies) with customized
849 emission filters (540/40 nm and 475/20 nm). Between 20-24 hrs post-transfection, the

850 cells were quickly washed before being incubated for 30 mins in 50 $\mu$L of modified Krebs-
851 Ringer buffer (containing 120 mM NaCl, 4.7 mM KCl, 2 mM $CaCl_2$, 0.7 mM $MgSO_4$,
852 10 mM glucose, 10 mM HEPES, and adjusted to pH 7.4) at 37°C in a $CO_2$-independent
853 incubator. After the pre-incubation period, the cell-permeable luciferase substrate,
854 coelenterazine h (40 $\mu$L, final concentration 5 $\mu$M), was added and the signal from the
855 mVenus fluorescence and nLuc luminescence were recorded using 485 and 530 nm
856 emission filters over a 45 min baseline BRET measurement (90 sec / cycle). Detection
857 time was always 500 ms for each wavelength. To ensure a stable baseline is achieved
858 following the substrate addition, BRET measurements are presented as the average
859 basal BRET signal over the final 30 minutes measurement interval (15-45 minutes). All
860 measurements were carried out in triplicate wells and repeated in three independent
861 experiments. From each well, the BRET ratio was calculated by dividing the 530 nm and
862 485 nm intensities, which were then normalized to an internal measurement of wells
863 transfected with the PM-PI4KA$^{BRET}$ biosensor alone.
864
865 ***Live-cell Confocal Microscopy of EGFP-PI4KA Localization***
866 HEK293A cells ($2.5x10^5$ cells/dish) were plated with a final volume of 1.5 mL on 29 mm
867 circular glass-bottom culture dishes (#1.5; Cellvis) pre-coated with 0.01% poly-L-lysine
868 solution (Sigma). Cells were allowed to attach overnight prior to transfection with plasmid
869 DNAs (0.5-0.75 µg/well) using Lipofectamine 2000 (2-5 µL/well; Invitrogen). Lipofection
870 was done using small volumes of Opti-MEM (200 µL; Invitrogen) according to the
871 manufacturer's instructions, once again with the slight modification of removing the media
872 containing the Lipofectamine-complexed DNA at 4-6 hrs post-transfection and replacing
873 it with complete DMEM. After 18-20 hrs of transfection, cells were incubated in 1 mL of
874 modified Krebs-Ringer solution (containing 120 mM NaCl, 4.7 mM KCl, 2 mM $CaCl_2$,
875 0.7 mM $MgSO_4$, 10 mM glucose, 10 mM HEPES, and adjusted to pH 7.4) and images
876 were acquired at room temperature using a Zeiss LSM 880 (63x/1.40 N.A. Plan-
877 Apochromat Oil DIC M27 Objective) laser-scanning confocal microscopes (Carl Zeiss
878 Microscopy). Image acquisition was performed using the ZEN software system (Carl

879 Zeiss Microscopy), while image preparation and analysis was done using the open-
880 source FIJI platform[166].
881

882 **References**


883 1. T. Balla, Phosphoinositides: tiny lipids with giant impact on cell regulation. *Physiol.*
884 *Rev.* **93**, 1019–1137 (2013).
885 2. J. E. Burke, J. Triscott, B. M. Emerling, G. R. V. Hammond, Beyond PI3Ks:
886 targeting phosphoinositide kinases in disease. *Nat Rev Drug Discov*, 1–30 (2022).
887 3. G. R. V. Hammond, J. E. Burke, Novel roles of phosphoinositides in signaling, lipid
888 transport, and disease. *Curr Opin Cell Biol* **63**, 57–67 (2020).
889 4. A. G. Batrouni, J. M. Baskin, The chemistry and biology of phosphatidylinositol 4-
890 phosphate at the plasma membrane. *Bioorg Med Chem* **40**, 116190 (2021).
891 5. F. Nakatsu, J. M. Baskin, J. Chung, L. B. Tanner, G. Shui, S. Y. Lee, M. Pirruccello,
892 M. Hao, N. T. Ingolia, M. R. Wenk, P. De Camilli, PtdIns4P synthesis by PI4KIIIα at
893 the plasma membrane and its impact on plasma membrane identity. *J. Cell Biol.*
894 **199**, 1003–1016 (2012).
895 6. J. Chung, F. Torta, K. Masai, L. Lucast, H. Czapla, L. B. Tanner, P.
896 Narayanaswamy, M. R. Wenk, F. Nakatsu, P. De Camilli, INTRACELLULAR
897 TRANSPORT. PI4P/phosphatidylserine countertransport at ORP5- and ORP8-
898 mediated ER-plasma membrane contacts. *Science* **349**, 428–432 (2015).
899 7. R. G. de Rubio, R. F. Ransom, S. Malik, D. I. Yule, A. Anantharam, A. V. Smrcka,
900 Phosphatidylinositol 4-phosphate is a major source of GPCR-stimulated
901 phosphoinositide production. *Sci Signal* **11**, eaan1210 (2018).
902 8. I. Barlow-Busch, A. L. Shaw, J. E. Burke, PI4KA and PIKfyve: Essential
903 phosphoinositide signaling enzymes involved in myriad human diseases. *Curr Opin*
904 *Cell Biol* **83**, 102207 (2023).
905 9. C. G. Salter, Y. Cai, B. Lo, G. Helman, H. Taylor, A. McCartney, J. S. Leslie, A.
906 Accogli, F. Zara, M. Traverso, J. Fasham, J. A. Lees, M. P. Ferla, B. A. Chioza, O.
907 Wenger, E. Scott, H. E. Cross, J. Crawford, I. Warshawsky, M. Keisling, D.
908 Agamanolis, C. Ward Melver, H. Cox, M. Elawad, T. Marton, M. N. Wakeling, D.
909 Holzinger, S. Tippelt, M. Munteanu, D. Valcheva, C. Deal, S. Van Meerbeke, C.
910 Walsh Vockley, M. J. Butte, U. Acar, M. S. van der Knaap, G. C. Korenke, U.
911 Kotzaeridou, T. Balla, C. Simons, H. H. Uhlig, A. H. Crosby, P. De Camilli, N. I.
912 Wolf, E. L. Baple, Biallelic PI4KA variants cause neurological, intestinal and
913 immunological disease. *Brain* **144**, 3597–3610 (2021).
914 10. E. Verdura, A. Rodríguez-Palmero, V. Vélez-Santamaria, L. Planas-Serra, I. de la
915 Calle, M. Raspall-Chaure, A. Roubertie, M. Benkirane, F. Saettini, L. Pavinato, G.
916 Mandrile, M. O'Leary, E. O'Heir, E. Barredo, A. Chacón, V. Michaud, C. Goizet, M.
917 Ruiz, A. Schlüter, I. Rouvet, J. Sala-Coromina, C. Fossati, M. Iascone, F.
918 Canonico, A. Marcé-Grau, P. de Souza, D. R. Adams, C. Casasnovas, H. L. Rehm,
919 H. C. Mefford, L. González Gutierrez-Solana, A. Brusco, M. Koenig, A. Macaya, A.
920 Pujol, Biallelic PI4KA variants cause a novel neurodevelopmental syndrome with
921 hypomyelinating leukodystrophy. *Brain* **144**, 2659–2669 (2021).

11. R. Chen, S. Giliani, G. Lanzi, G. I. Mias, S. Lonardi, K. Dobbs, J. Manis, H. Im, J. E. Gallagher, D. H. Phanstiel, G. Euskirchen, P. Lacroute, K. Bettinger, D. Moratto, K. Weinacht, D. Montin, E. Gallo, G. Mangili, F. Porta, L. D. Notarangelo, S. Pedretti, W. Al-Herz, W. Alfahdli, A. M. Comeau, R. S. Traister, S.-Y. Pai, G. Carella, F. Facchetti, K. C. Nadeau, M. Snyder, L. D. Notarangelo, Whole-exome sequencing identifies tetratricopeptide repeat domain 7A (TTC7A) mutations for combined immunodeficiency with intestinal atresias. *J. Allergy Clin. Immunol.* **132**, 656-664.e17 (2013).
12. A. E. Bigorgne, H. F. Farin, R. Lemoine, N. Mahlaoui, N. Lambert, M. Gil, A. Schulz, P. Philippet, P. Schlesser, T. G. Abrahamsen, K. Oymar, E. G. Davies, C. L. Ellingsen, E. Leteurtre, B. Moreau-Massart, D. Berrebi, C. Bole-Feysot, P. Nischke, N. Brousse, A. Fischer, H. Clevers, G. de Saint Basile, TTC7A mutations disrupt intestinal epithelial apicobasal polarity. *J Clin Invest* **124**, 328–337 (2014).
13. H. Adhikari, W. E. Kattan, S. Kumar, P. Zhou, J. F. Hancock, C. M. Counter, Oncogenic KRAS is dependent upon an EFR3A-PI4KA signaling axis for potent tumorigenic activity. *Nat Commun* **12**, 5248 (2021).
14. W. E. Kattan, J. Liu, D. Montufar-Solis, H. Liang, B. Brahmendra Barathi, R. van der Hoeven, Y. Zhou, J. F. Hancock, Components of the phosphatidylserine endoplasmic reticulum to plasma membrane transport mechanism as targets for KRAS inhibition in pancreatic cancer. *Proc Natl Acad Sci USA* **118**, e2114126118 (2021).
15. K. L. Berger, J. D. Cooper, N. S. Heaton, R. Yoon, T. E. Oakland, T. X. Jordan, G. Mateu, A. Grakoui, G. Randall, Roles for endocytic trafficking and phosphatidylinositol 4-kinase III alpha in hepatitis C virus replication. *Proc. Natl. Acad. Sci. U.S.A.* **106**, 7577–7582 (2009).
16. J. E. Burke, Structural Basis for Regulation of Phosphoinositide Kinases and Their Involvement in Human Disease. *Mol. Cell* **71**, 653–673 (2018).
17. J. A. Lees, Y. Zhang, M. S. Oh, C. M. Schauder, X. Yu, J. M. Baskin, K. Dobbs, L. D. Notarangelo, P. De Camilli, T. Walz, K. M. Reinisch, Architecture of the human PI4KIIIα lipid kinase complex. *Proc. Natl. Acad. Sci. U.S.A.* **114**, 13720–13725 (2017).
18. J. M. Baskin, X. Wu, R. Christiano, M. S. Oh, C. M. Schauder, E. Gazzerro, M. Messa, S. Baldassari, S. Assereto, R. Biancheri, F. Zara, C. Minetti, A. Raimondi, M. Simons, T. C. Walther, K. M. Reinisch, P. De Camilli, The leukodystrophy protein FAM126A (hyccin) regulates PtdIns(4)P synthesis at the plasma membrane. *Nat. Cell Biol.* **18**, 132–138 (2016).
19. S. Suresh, J. E. Burke, Structural basis for the conserved roles of PI4KA and its regulatory partners and their misregulation in disease. *Adv Biol Regul* **90**, 100996 (2023).
20. G. L. Dornan, U. Dalwadi, D. J. Hamelin, R. M. Hoffmann, C. K. Yip, J. E. Burke, Probing the Architecture, Dynamics, and Inhibition of the PI4KIIIα/TTC7/FAM126 Complex. *J. Mol. Biol.* **430**, 3129–3142 (2018).

21. N. Bojjireddy, M. L. Guzman-Hernandez, N. R. Reinhard, M. Jovic, T. Balla, EFR3s are palmitoylated plasma membrane proteins that control responsiveness to G protein-coupled receptors. *J. Cell. Sci.*, doi: 10.1242/jcs.157495 (2014).
22. A. G. Batrouni, N. Bag, H. T. Phan, B. A. Baird, J. M. Baskin, A palmitoylation code controls PI4KIIIα complex formation and PI(4,5)P2 homeostasis at the plasma membrane. *J Cell Sci* **135**, jcs259365 (2022).
23. D. Baird, C. Stefan, A. Audhya, S. Weys, S. D. Emr, Assembly of the PtdIns 4-kinase Stt4 complex at the plasma membrane requires Ypp1 and Efr3. *J. Cell Biol.* **183**, 1061–1074 (2008).
24. X. Wu, R. J. Chi, J. M. Baskin, L. Lucast, C. G. Burd, P. De Camilli, K. M. Reinisch, Structural insights into assembly and regulation of the plasma membrane phosphatidylinositol 4-kinase complex. *Developmental Cell* **28**, 19–29 (2014).
25. J. Myeong, L. de la Cruz, S.-R. Jung, J.-H. Yeon, B.-C. Suh, D.-S. Koh, B. Hille, Phosphatidylinositol 4,5-bisphosphate is regenerated by speeding of the PI 4-kinase pathway during long PLC activation. *J Gen Physiol* **152**, e202012627 (2020).
26. J. Jumper, R. Evans, A. Pritzel, T. Green, M. Figurnov, O. Ronneberger, K. Tunyasuvunakool, R. Bates, A. Žídek, A. Potapenko, A. Bridgland, C. Meyer, S. A. A. Kohl, A. J. Ballard, A. Cowie, B. Romera-Paredes, S. Nikolov, R. Jain, J. Adler, T. Back, S. Petersen, D. Reiman, E. Clancy, M. Zielinski, M. Steinegger, M. Pacholska, T. Berghammer, S. Bodenstein, D. Silver, O. Vinyals, A. W. Senior, K. Kavukcuoglu, P. Kohli, D. Hassabis, Highly accurate protein structure prediction with AlphaFold. *Nature* **596**, 583–589 (2021).
27. M. Mirdita, K. Schütze, Y. Moriwaki, L. Heo, S. Ovchinnikov, M. Steinegger, ColabFold: making protein folding accessible to all. *Nat Methods* **19**, 679–682 (2022).
28. E. I. James, T. A. Murphree, C. Vorauer, J. R. Engen, M. Guttman, Advances in Hydrogen/Deuterium Exchange Mass Spectrometry and the Pursuit of Challenging Biological Systems. *Chem Rev* **122**, 7562–7623 (2022).
29. G. R. Masson, M. L. Jenkins, J. E. Burke, An overview of hydrogen deuterium exchange mass spectrometry (HDX-MS) in drug discovery. *Expert Opin Drug Discov* **12**, 981–994 (2017).
30. G. R. Masson, J. E. Burke, N. G. Ahn, G. S. Anand, C. Borchers, S. Brier, G. M. Bou-Assaf, J. R. Engen, S. W. Englander, J. Faber, R. Garlish, P. R. Griffin, M. L. Gross, M. Guttman, Y. Hamuro, A. J. R. Heck, D. Houde, R. E. Iacob, T. J. D. Jørgensen, I. A. Kaltashov, J. P. Klinman, L. Konermann, P. Man, L. Mayne, B. D. Pascal, D. Reichmann, M. Skehel, J. Snijder, T. S. Strutzenberg, E. S. Underbakke, C. Wagner, T. E. Wales, B. T. Walters, D. D. Weis, D. J. Wilson, P. L. Wintrode, Z. Zhang, J. Zheng, D. C. Schriemer, K. D. Rand, Recommendations for performing, interpreting and reporting hydrogen deuterium exchange mass spectrometry (HDX-MS) experiments. *Nat. Methods* **16**, 595–602 (2019).
31. I. Ulengin-Talkish, M. A. H. Parson, M. L. Jenkins, J. Roy, A. Z. L. Shih, N. St-Denis, G. Gulyas, T. Balla, A.-C. Gingras, P. Várnai, E. Conibear, J. E. Burke, M. S. Cyert, Palmitoylation targets the calcineurin phosphatase to the

1008 phosphatidylinositol 4-kinase complex at the plasma membrane. *Nat Commun* **12**,
1009 6064 (2021).
1010 32. N. S. Agarwal, L. Northrop, K. Anyane-Yeboa, V. S. Aggarwal, P. L. Nagy, Y. Y.
1011 Demirdag, Tetratricopeptide repeat domain 7A (TTC7A) mutation in a newborn with
1012 multiple intestinal atresia and combined immunodeficiency. *J. Clin. Immunol.* **34**,
1013 607–610 (2014).
1014 33. S. Jardine, N. Dhingani, A. M. Muise, TTC7A: Steward of Intestinal Health. *Cell Mol*
1015 *Gastroenterol Hepatol* **7**, 555–570 (2019).
1016 34. M. Varadi, S. Anyango, M. Deshpande, S. Nair, C. Natassia, G. Yordanova, D.
1017 Yuan, O. Stroe, G. Wood, A. Laydon, A. Žídek, T. Green, K. Tunyasuvunakool, S.
1018 Petersen, J. Jumper, E. Clancy, R. Green, A. Vora, M. Lutfi, M. Figurnov, A. Cowie,
1019 N. Hobbs, P. Kohli, G. Kleywegt, E. Birney, D. Hassabis, S. Velankar, AlphaFold
1020 Protein Structure Database: massively expanding the structural coverage of
1021 protein-sequence space with high-accuracy models. *Nucleic Acids Research* **50**,
1022 D439–D444 (2022).
1023 35. P. V. Hornbeck, B. Zhang, B. Murray, J. M. Kornhauser, V. Latham, E. Skrzypek,
1024 PhosphoSitePlus, 2014: mutations, PTMs and recalibrations. *Nucleic Acids Res.*
1025 **43**, D512-20 (2015).
1026 36. J. Chung, F. Nakatsu, J. M. Baskin, P. De Camilli, Plasticity of PI4KIIIα interactions
1027 at the plasma membrane. *EMBO Rep.* **16**, 312–320 (2015).
1028 37. Y. Perez-Riverol, J. Bai, C. Bandla, D. García-Seisdedos, S. Hewapathirana, S.
1029 Kamatchinathan, D. J. Kundu, A. Prakash, A. Frericks-Zipper, M. Eisenacher, M.
1030 Walzer, S. Wang, A. Brazma, J. A. Vizcaíno, The PRIDE database resources in
1031 2022: a hub for mass spectrometry-based proteomics evidences. *Nucleic Acids*
1032 *Res* **50**, D543–D552 (2022).
1033 38. D. G. Gibson, L. Young, R.-Y. Chuang, J. C. Venter, C. A. Hutchison, H. O. Smith,
1034 Enzymatic assembly of DNA molecules up to several hundred kilobases. *Nat.*
1035 *Methods* **6**, 343–345 (2009).
1036 39. J. T. Tóth, G. Gulyás, D. J. Tóth, A. Balla, G. R. V. Hammond, L. Hunyady, T.
1037 Balla, P. Várnai, BRET-monitoring of the dynamic changes of inositol lipid pools in
1038 living cells reveals a PKC-dependent PtdIns4P increase upon EGF and M3
1039 receptor activation. *Biochim Biophys Acta* **1861**, 177–187 (2016).
1040 40. Z. Liu, O. Chen, J. B. J. Wall, M. Zheng, Y. Zhou, L. Wang, H. R. Vaseghi, L. Qian,
1041 J. Liu, Systematic comparison of 2A peptides for cloning multi-genes in a
1042 polycistronic vector. *Sci Rep* **7**, 2193 (2017).
1043 41. G. R. V. Hammond, M. P. Machner, T. Balla, A novel probe for phosphatidylinositol
1044 4-phosphate reveals multiple pools beyond the Golgi. *J Cell Biol* **205**, 113–126
1045 (2014).
1046 42. E. F. Pettersen, T. D. Goddard, C. C. Huang, G. S. Couch, D. M. Greenblatt, E. C.
1047 Meng, T. E. Ferrin, UCSF Chimera--a visualization system for exploratory research
1048 and analysis. *J Comput Chem* **25**, 1605–1612 (2004).
1049 43. P. V. Afonine, R. W. Grosse-Kunstleve, N. Echols, J. J. Headd, N. W. Moriarty, M.
1050 Mustyakimov, T. C. Terwilliger, A. Urzhumtsev, P. H. Zwart, P. D. Adams, Towards

automated crystallographic structure refinement with phenix.refine. *Acta Crystallogr. D Biol. Crystallogr.* **68**, 352–367 (2012).

44. J. T. B. Stariha, R. M. Hoffmann, D. J. Hamelin, J. E. Burke, Probing Protein-Membrane Interactions and Dynamics Using Hydrogen-Deuterium Exchange Mass Spectrometry (HDX-MS). *Methods Mol Biol* **2263**, 465–485 (2021).
45. J. M. Dobbs, M. L. Jenkins, J. E. Burke, Escherichia coli and Sf9 Contaminant Databases to Increase Efficiency of Tandem Mass Spectrometry Peptide Identification in Structural Mass Spectrometry Experiments. *J Am Soc Mass Spectrom* **31**, 2202–2209 (2020).
46. A. T. Kong, F. V. Leprevost, D. M. Avtonomov, D. Mellacheruvu, A. I. Nesvizhskii, MSFragger: ultrafast and comprehensive peptide identification in mass spectrometry-based proteomics. *Nat Methods* **14**, 513–520 (2017).
47. P. Gouet, X. Robert, E. Courcelle, ESPript/ENDscript: Extracting and rendering sequence and 3D information from atomic structures of proteins. *Nucleic Acids Res.* **31**, 3320–3323 (2003).

# Supplementary Figures and Tables

A

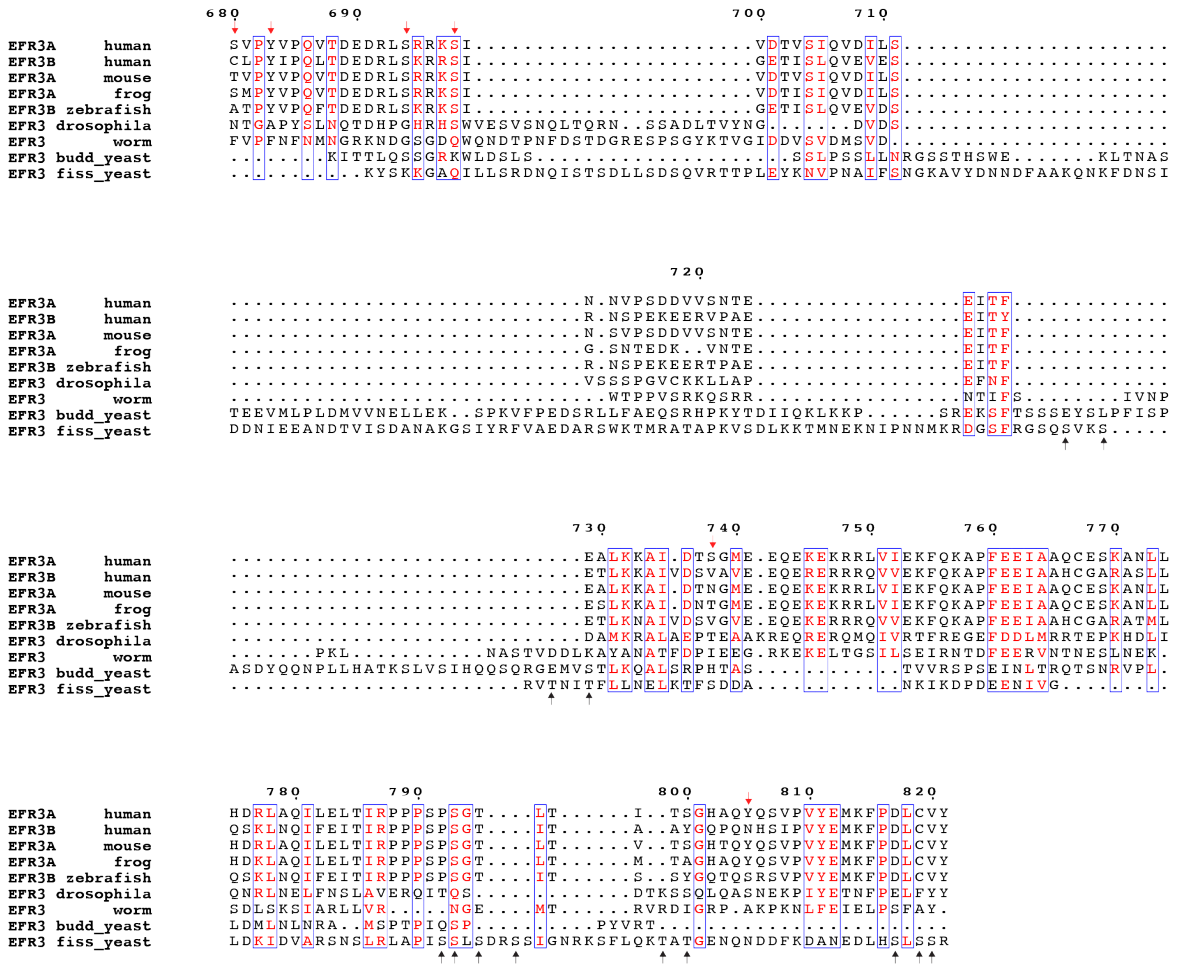


**Supplemental Figure 1: EFR3 C-terminal tail sequence alignment**

**A.** Multiple sequence alignment (generated with ESPript 3.0) of EFR3 from *Homo sapiens, Mus musculus, Xenopus laevis, Danio rerio, Drosophila melanogaster, Caenorhabditis elegans*, *Schizosaccharomyces pombe,* and *Saccharomyces cerevisiae.* Human EFR3A residues that are reported phosphorylation sites (Phosphosite) are annotated above in red. Yeast efr3 residues that are reported phosphorylation sites (PhosphoGRID) are annotated below in black.

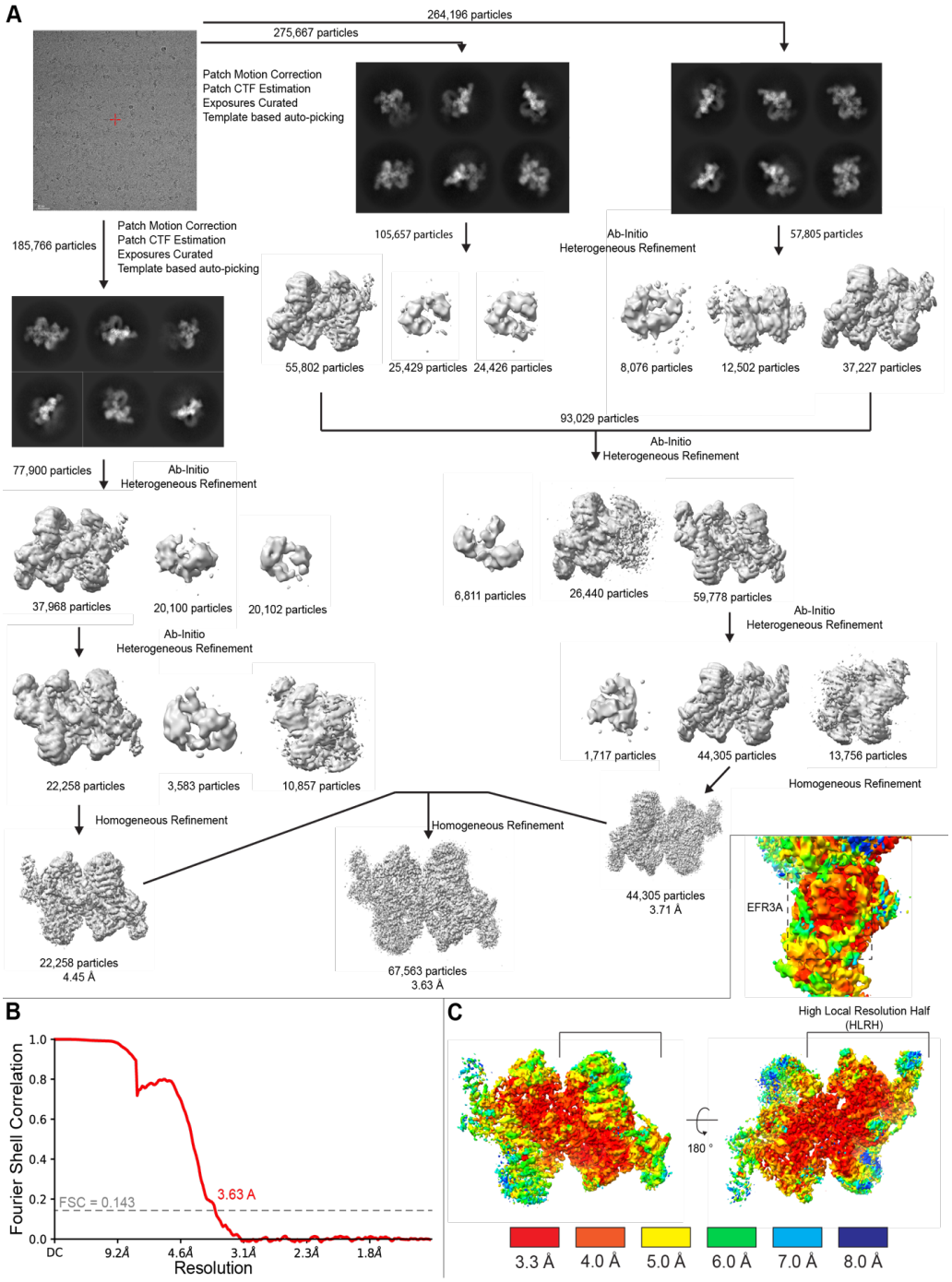


**Supplemental Figure 2 (related to Fig.1): Cryo-EM data processing**

**A.** Cryo-EM data processing workflow showing a representative micrograph from screening on the 200 kV Glacios, representative 2D class averages, and the image processing strategy used to generate a 3D reconstruction of the PI4KA/TTC7B/FAM126A/EFR3A complex.

**B.** Gold standard Fourier shell correlation coefficient (FSC) curve after auto tightening by cryoSPARC for the final map.

**C.** Final map coloured according to local resolution estimated using cryoSPARC v4.2.1, with a zoom-in of the EFR3A density.

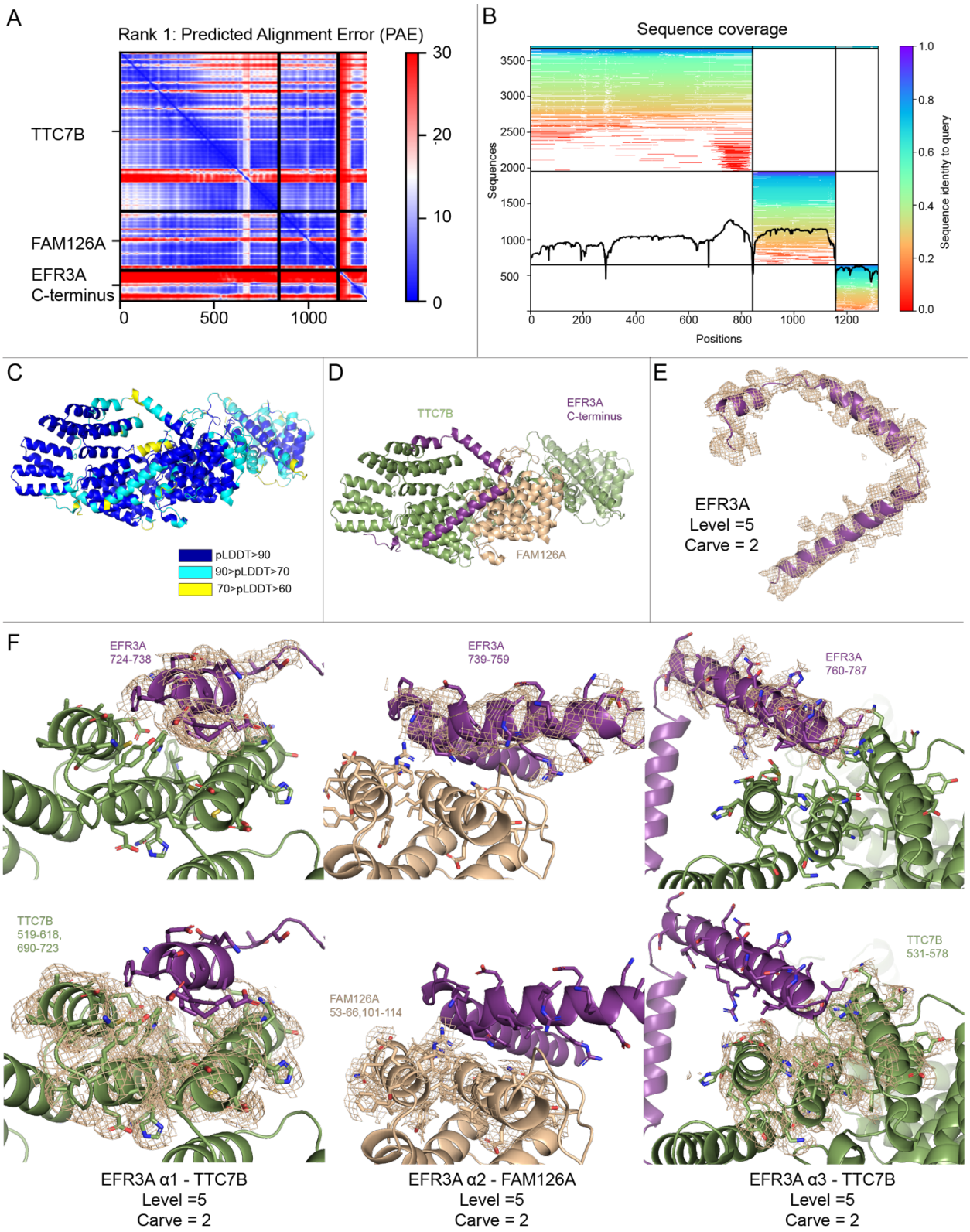


**Supplemental Figure 3: Model building with AlphaFold Multimer and map to model density fit**
**A.** Predicted aligned error (PAE) of the AlphaFold Multimer prediction of the TTC7B-FAM126A and EFR3A C-terminus.

1116 **B.** Sequence coverage from Multiple Sequence Alignment performed by AlphaFold Multimer for each
1117 inputted protein primary sequence.
1118 **C.** AlphaFold Multimer model of the TTC7B-FAM126A in complex with EFR3A C-terminus with the per-
1119 residue confidence metric predicted local-distance difference test (pLDDT) <60 removed, coloured
1120 according to pLDDT score.
1121 **D.** AlphaFold Multimer model of the TTC7B-FAM126A in complex with EFR3A C-terminal with the per-
1122 residue confidence metric predicted local-distance difference test (pLDDT) <60 removed.
1123 **E.** Electron density of EFR3A C-terminus.
1124 **F.** Electron density of selected regions. (L) EFR3A $\alpha$1- TTC7B interface, with density for EFR3A (724-738)
1125 shown on top, and the density for the TTC7B interface helices (519-618, 690-723) shown on bottom (M)
1126 EFR3A $\alpha$2- FAM126A interface, with density for EFR3A (739-759) shown on top, and the density for the
1127 FAM126A interface helices (53-66,101-114) shown on bottom, and (R) EFR3A $\alpha$3- TTC7B interface, with
1128 density for EFR3A (760-787) shown on top, and the density for the TTC7B interface helices (531-578)
1129 shown on bottom.
1130

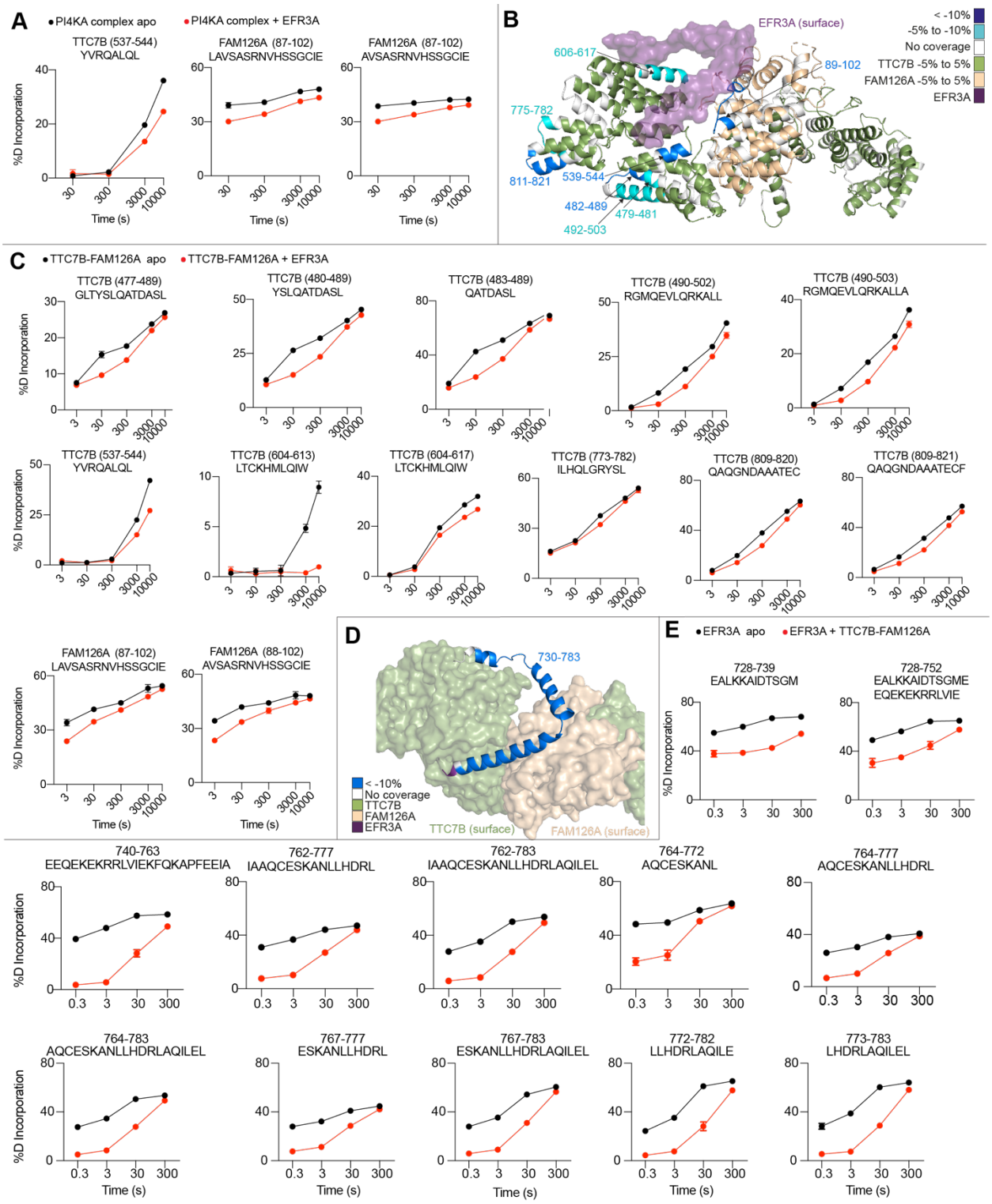


**Supplemental Figure 4: Raw HDX-MS deuterium incorporation curves**

**A.** Relative deuterium incorporation traces for peptides showing significant differences in deuterium exchange (defined as >5% >0.45 Da, and p>0.01 in an unpaired two-tailed t-test at any time point) upon PI4KA complex binding to EFR3A.

1136 **B.** Significant differences in deuterium exchange (defined as >5% >0.45 Da, and p>0.01 in an unpaired
1137 two-tailed t-test at any time point) upon TTC7B-FAM126A dimer binding to EFR3A with all regions
1138 annotated.
1139 **C.** Relative deuterium incorporation traces for peptides showing significant differences in deuterium
1140 exchange (defined as >5% >0.45 Da, and p>0.01 in an unpaired two-tailed t-test at any time point) upon
1141 TTC7B-FAM126A dimer binding to EFR3A.
1142 **D.** Significant differences in deuterium exchange (defined as >5% >0.45 Da, and p>0.01 in an unpaired
1143 two-tailed t-test at any time point) upon MBP-EFR3A binding to the TTC7B-FAM126A dimer with all regions
1144 annotated.
1145 **E.** Relative deuterium incorporation traces for peptides showing significant differences in deuterium
1146 exchange (defined as >5% >0.45 Da, and p>0.01 in an unpaired two-tailed t-test at any time point) upon
1147 MBP-EFR3A binding to the TTC7B-FAM126A dimer.
1148
1149
1150
1151
1152
1153

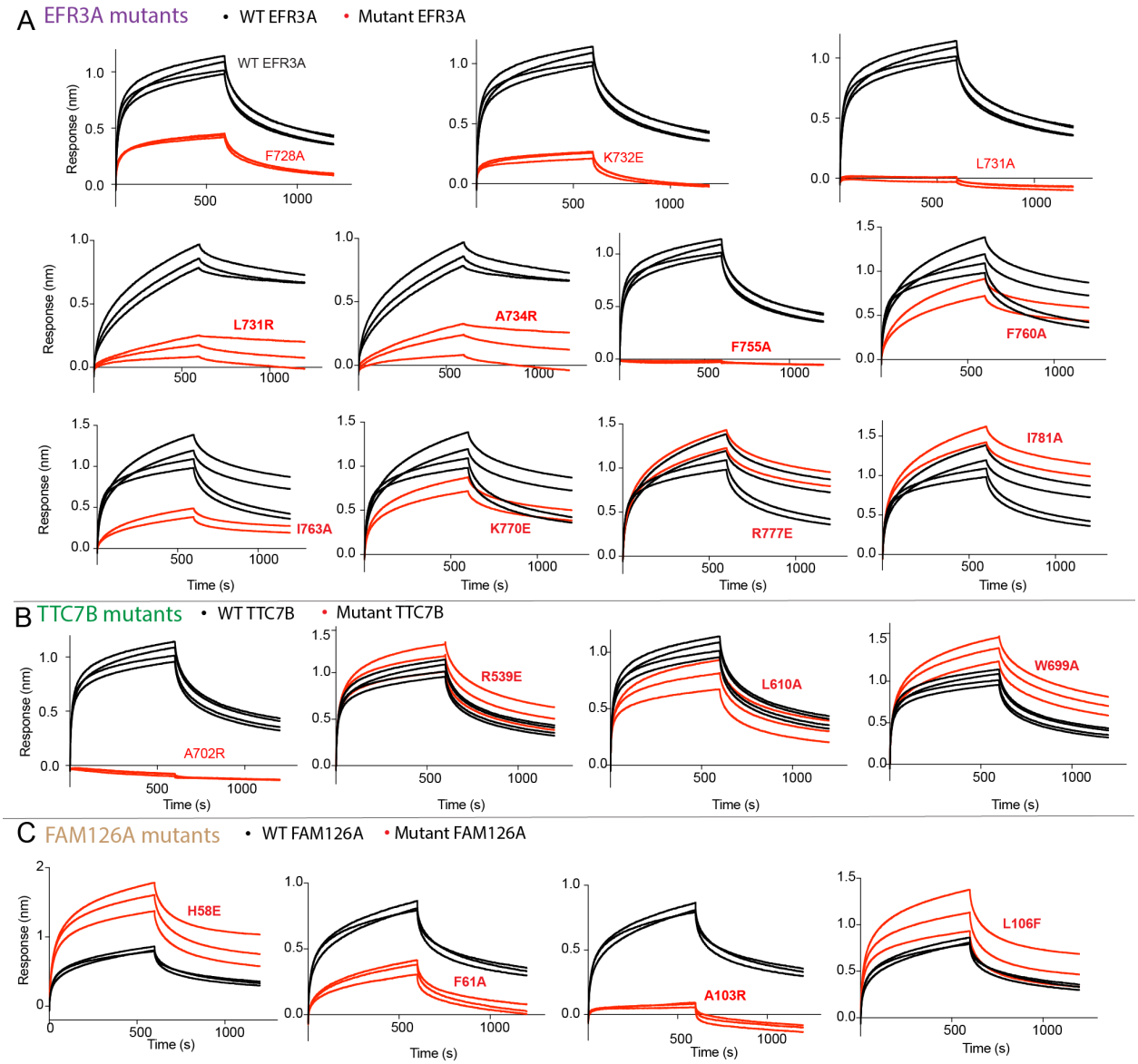


**Supplemental Figure 5: BLI raw data**

**A.** Raw BLI association and dissociation curves of all EFR3A mutants (shown in table S2) compared to WT. His-EFR3A was loaded on the anti-penta-His tip at 200 nM and dipped in TTC7B-FAM126A at 500 nM.
**B.** Raw BLI association and dissociation curves of all TTC7B mutants (shown in table S2) compared to WT. His-EFR3A was loaded on the anti-penta-His tip at 200 nM and dipped in TTC7B-FAM126A at 500 nM.
**C.** Raw BLI association and dissociation curves of all TTC7B mutants (shown in table S2) compared to WT. His-EFR3A was loaded on the anti-penta-His tip at 200 nM and dipped in TTC7B-FAM126A at 500 nM.

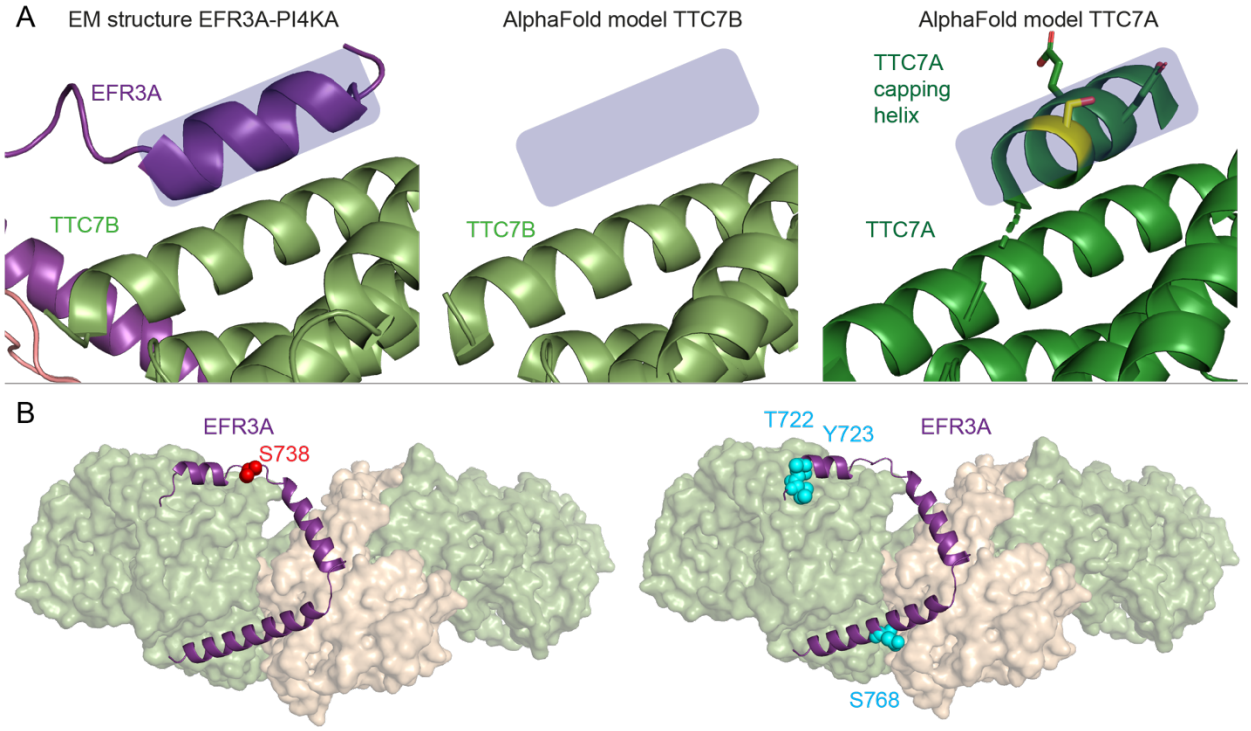


**Supplemental Figure 6: Differences between TTC7A/TTC7B and post-translational modification sites present at the EFR3-TTC7-FAM126 interface**

**A.** The structure of the α1 helix of EFR3A bound to TTC7B is shown on the top left. The AlphaFold models of TTC7B (middle) and TTC7A (right) are shown with all very low confidence regions (pLDDT values less than 50 being removed). AlphaFold predicts a capping helix in TTC7A at this binding interface, which has a reported phosphorylation site (Phosphosite) at S690 (colored yellow in the right panel). Additional reported TTC7A phosphorylation sites (Phosphosite) near this site are in predicted unstructured regions include S647, S678, S679, and T693.

**B.** (L) EFR3A and (R) EFR3B phosphorylation sites (Phosphosite) mapped on the cryo-EM model of PI4KA complex-EFR3A C-terminus.

1193 **Table S1 Cryo-EM data collection, refinement, and validation statistics**

| | PI4KA/TTC7B/FAM126A (1-308)-EFR3A C-terminus<br>EMD- 44413<br>PDB:9BAX |
|---|---|
| **Data collection and processing** | |
| Magnification | 165,000 |
| Voltage (kV) | 300 |
| Electron exposure (e/ Å$^2$) | 50 |
| Defocus range ($\mu$M) | 0.5-2.0 |
| Pixel size (Å) | 0.77 |
| Symmetry imposed | C1 |
| Initial particle images (no.) | 725,629 |
| Final particle images (no.) | 67,563 |
| Map resolution (Å) | 3.63 |
| FSC threshold | 0.143 |
| Map resolution range (Å) | 3.3-10 |
| | |
| **Refinement** | |
| Initial model used (PDB) | 6BQ1 |
| Model Resolution (Å) | 3.63 |
| FSC threshold | 0.143 |
| Map sharpening B factor | |
| Model composition | |
| Non-hydrogen atoms | 43806 |
| Protein residues | 5482 |
| Ligands | 0 |
| *B*-factors | |
| Protein | 237.1 |
| Validation | |
| Mol probability score | 2.39 |
| Clashscore | 12.88 |
| Poor rotamers (%) | 2.8 |
| Ramachandran | |
| Favoured | 93.3 |
| Allowed | 6.7 |
| Outliers | 0.02 |
| R.M.S. deviations | |
| Bond lengths (Å) | 0.005 |
| Bond angles (°) | 0.655 |

1194

1195 **Table S2 Key Reagent/Resources**

| REAGENT or RESOURCE | SOURCE | IDENTIFIER |
|---|---|---|
| **Bacterial and virus strains** | | |

| | | |
|---|---|---|
| *E.coli* XL10-GOLD KanR Ultracompetent Cells | Agilent | 200317 |
| *E.coli* DH10EMBacY Competent Cells | Geneva Biotech | DH10EMBacY |
| C41(DE3) chemically competent cells | Lab stock | |
| **Chemicals, peptides, and recombinant proteins** | | |
| Deuterium Oxide 99.9% | Sigma Aldrich | 151882-10X1ML |
| $BS^3$ | Thermo Fischer Scientific | 21580 |
| ATP | Sigma | A7699-1g |
| $MgCl_2$ | Caledon Laboratory Chemicals | 4720-1 |
| **Deposited Data** | | |
| Mass spectrometry proteomics data | https://www.ebi.ac.uk/pride/ | PXD043442 |
| PDB | https://www.rcsb.org/ | 9BAX |
| EMDB | https://www.emdataresource.org/ | 44413 |
| **Recombinant DNA** | | |
| PI4KA Complex | Dornan et al., 2018 | GD177 |
| EFR3A (721-791) | This paper | SS77 |
| MBP-EFR3A (721-791) | This paper | MJ319 |
| EFR3A (F728A) | This paper | SS88 |
| EFR3A (L731A) | This paper | SS99 |
| EFR3A (L731R) | This paper | SS140 |
| EFR3A (L734R) | This paper | SS141 |
| EFR3A (K732E) | This paper | SS89 |
| EFR3A (F755A) | This paper | SS90 |
| EFR3A (F760A) | This paper | SS91 |
| EFR3A (I763A) | This paper | SS102 |
| EFR3A (K770E) | This paper | SS92 |
| EFR3A (R777E) | This paper | SS93 |
| EFR3A (I781A) | This paper | SS94 |
| TTC7B-FAM126A (1-308) WT | Dornan et al., 2018 | GD176 |
| TTC7B-FAM126A (1-308) WT – *E.coli* | This paper | AS29 |
| TTC7B (A702R)-FAM126A (1-308) | This paper | MS8 |
| TTC7B (R539E)-FAM126A (1-308) | This paper | SS115 |
| TTC7B (L610A)-FAM126A (1-308) | This paper | SS113 |
| TTC7B (W699A)-FAM126A (1-308) | This paper | SS116 |
| TTC7B-FAM126A (H58E) (2-308) | This paper | SS104 |
| TTC7B-FAM126A (F61A) (1-308) | This paper | SS103 |
| TTC7B-FAM126A (A103R) (1-308) | This paper | MS4 |
| TTC7B-FAM126A (L106F) (1-308) | This paper | SS105 |
| EFR3Bha_gsgT2A_TTC7Bmyc_FlagFam126A | This paper | C3 |
| EFR3Bha_t2a_TTC7B myc_p2a_Flag FAM126A (A103R) | This paper | NH74 |
| EFR3Bha_t2a_TTC7B (A702R) myc_p2a_Flag FAM126A | This paper | NH75 |
| EFR3Bha (del 721-791)_gsgT2A_TTC7Bmyc_FlagFam126A | This paper | NH93 |
| EFR3Bha(L727A, F751A)_gsgT2A_TTC7Bmyc_FlagFam126A | This paper | NH94 |

| | | |
|---|---|---|
| EGFP-PI4KA | Hammond et al., 2014 | |
| L10-mVenus-tPT2A-nLuc-PI4KA | This paper | PM-PI4KA$^{BRET}$ |
| **Software and algorithms** | | |
| cryoSPARC v4.2.1 | Structura Bio | https://cryosparc.com |
| Phenix-1.19.1 | Open source | https://phenix-online.org/ |
| COOT-0.9.4.1 | CCP4 | https://www2.mrc-lmb.ca |
| HDExaminer | Sierra Analytics | http://massspec.com/hdexaminer |
| Bruker Compass DataAnalysis 4.2 | Bruker | http://www.bruker.com |
| GraphPad Prism 7 | GraphPad | https://www.graphpad.com |
| PEAKS 7 | Bioinformatics Solutions Inc. | https://www.bioinfor.com/versions/ |
| FragPipe (v19.1) | Nesvizhskii Lab – University of Michigan | fragpipe.nesvilab.org |
| Adobe Illustrator 2021 | Adobe | https://www.adobe.com/products/illustrator.html |
| ESPript 3.0 | SBGrid consortium | https:espript.ibcp.fr |
| PyMOL | Schroedinger | http://pymol.org |
| ChimeraX | UCSF | https://www.cgl.ucsf.edu/chimerax/ |
| **Other** | | |
| C-flat Holey Thick Carbon Grid 2.0 $\mu$m hole 1.0 $\mu$m space 300 mesh | Electron Microscopy Studies | CFT312-100 |
| SF9 insect cells for expression | Expression Systems | 94-001S |
| Octet HIS1K Biosensors | Sartorius | 18-5120 |
| Enzymate Protein Pepsin Column, 300Å, 5$\mu$m, 2.1 mm X 30 mm | Waters | 186007233 |
| ProDx Pepsin Column F 10-32 | Trajan Scientific Americas | 359997870 |
| ACQUITY UPLC BEH C18 1.7 $\mu$m, 2.1 mm x 5 mm | Waters | 186004629 |
| ACQUITY UPLC Peptide BEH C18 Column, 300Å, 1.7 $\mu$m, 100 mm X 2.1 mm | Waters | 186003686 |

1196